Monthly Notices of the ROYAL ASTRONOMICAL SOCIETY

MNRAS **541,** 1649–1669 (2025) https://doi.org/10.1093/mnras/staf1065
Advance Access publication 2025 July 1

Collapse of rotating white dwarfs and multimessenger signals

Takami Kuroda [1]★ Kyohei Kawaguchi [1,2] and Masaru Shibata[1,2]

[1]*Department of Computational Relativistic Astrophysics, Max-Planck-Institut für Gravitationsphysik, Am Mühlenberg 1, D-14476 Potsdam-Golm, Germany*
[2]*Center for Gravitational Physics and Quantum-Information, Yukawa Institute for Theoretical Physics, Kyoto University, Kyoto 606-8502, Japan*

Accepted 2025 June 21. Received 2025 June 2; in original form 2025 March 21

ABSTRACT

We present results of numerical relativity simulations for the collapse of rotating magnetized white dwarfs (WDs) in three dimension, aiming at discussing the explosion dynamics and associate multimessenger signals: gravitational waves (GWs), neutrinos, and electromagnetic counterparts. All WDs initiate gravitational collapse due to electron captures and then experience prompt-type explosions after the proto-neutron star formation. We observe the explosions dominated by a bipolar structure and the emergence of strong spiral waves in rapidly rotating models. The spiral waves facilitate to increase both the explosion energy and ejecta mass, though the final values still fall in the category of low explosion energy supernovae with small ejecta mass. The spiral waves also produce strong GWs, which may expand the horizon distance of such events against GWs up to $\sim 10\,\mathrm{Mpc}$ for third-generation ground-based detectors. Additionally as an intriguing implication, we demonstrate that such accretion or merger-induced collapse of WDs might be able to explain some of the rapidly evolving optical transients, such as fast blue optical transients (FBOTs), as previously suggested. Based on the simulation results together with several assumptions, we confirm that the magnetar may account for the brighter side of some of observed FBOTs, while a combination of ejecta-envelope interaction which can be also followed by radioactive decay of heavy elements synthesized along with the explosion might still explain the fainter branch even in the absence of magnetar formation.

Key words: (stars:) supernovae: general – stars: neutron – gravitational waves – neutrinos – (magnetohydrodynamics) MHD.

1 INTRODUCTION

The nature of lower ejecta mass in accretion- or merger-induced collapse (AIC/MIC) of white dwarfs (WDs) could be the key to understanding rapidly evolving transients, whose features are hardly interpreted by standard supernovae (SNe). WDs in a binary system may acquire mass from its non-degenerate companion star (Nomoto, Nariai & Sugimoto 1979; Nomoto & Kondo 1991) or through a merger with its companion WD (Saio & Nomoto 1985; Shen et al. 2012; Schwab 2021). Depending on the mass accretion history, WDs can avoid a violent nuclear burning, i.e. Type Ia SNe, and steadily increases both their mass and central density. Once the WD mass exceeds the Chandrasekhar mass and its central density achieves a sufficiently high value ($\sim 10^{10}\,\mathrm{g\,cm^{-3}}$), electron capture takes place at its centre, which triggers a collapse of WDs to a neutron star (NS) and subsequent explosion, namely electron capture SN (ECSN; Nomoto & Kondo 1991; Yoon & Langer 2005).

ECSNe of WDs – hereafter we simply term them as AICs regardless of whether the WD gains mass from a non-degenerate (AIC) or degenerate companion star (MIC) – are characterized by their relatively low ejecta mass. This is a natural consequence of the initially *low* total mass of the system, i.e. the WD mass at the Chandrasekhar limit, which practically ranges from $\sim 1.4\,\mathrm{M_\odot}$ for a non-spinning WD to $\lesssim 2\,\mathrm{M_\odot}$ for a rapidly rotating one depending also on the actual evolutionary path (e.g. Yoon & Langer 2005). As the ejecta mass is at most the difference between initial WD and remnant NS masses, the expected ejecta mass ($M_{\rm ej}$) is obviously quite low, typically $M_{\rm ej} \lesssim$ a few times of $0.1\,\mathrm{M_\odot}$. Such values are at least one order of magnitude smaller than the canonical values for Type II/Ibc SNe associated with the massive stellar collapse. Furthermore, the absence of massive WD envelopes generally avoids the deceleration of ejecta and keeps the ejecta velocities nearly at their original high values, which could be another noteworthy feature of AICs.

During the evolutionary phase of WDs, they may acquire some unique properties, which result in the formation of a remnant NS having distinct features. The most important is stemming from spinning up of WDs via the mass accretion from a companion star (Yoon & Langer 2005; Di Stefano, Voss & Claeys 2011) or merger with a companion WD (Hachisu, Eriguchi & Nomoto 1986; Segretain, Chabrier & Mochkovitch 1997; Marsh, Nelemans & Steeghs 2004; Dan et al. 2014). For instance, Yoon & Langer (2005) proposed that some WDs can increase their angular frequencies to $\gtrsim$ a few $\mathrm{rad\,s^{-1}}$ by mass accretion from its companion. In addition these WDs may avoid the path towards the Type Ia SN branch, though the detailed evolutionary paths depend on various effects, such as rotational instabilities, magnetic torque, and viscous effects between the WD and its surrounding disc (e.g. Saio & Nomoto 2004). If the core of WDs gains such high angular frequencies ($\sim$ a few $\mathrm{rad\,s^{-1}}$) at the onset of an AIC, it is enough to produce a rapidly rotating NS, whose angular frequency reaches $\gtrsim 1000\,\mathrm{rad\,s^{-1}}$.

In addition, the merger of two WDs may often amplify the seed magnetic fields to strong values (Tout et al. 2008; García-Berro

★ E-mail: takami.kuroda@aei.mpg.de

et al. 2012). Indeed, the existence of strongly magnetized WDs, whose surface magnetic fields reach in some cases $\sim 10^{8-9}$ G, are observationally confirmed both in isolated and binary WDs (Wickramasinghe & Ferrario 2000; Schmidt et al. 2003). Numerical simulations of merging WDs also support the formation of such strongly magnetized WDs (Zhu et al. 2015). Assuming a simple dipole-like magnetic field configuration, the core magnetic fields of the observed strongly magnetized WDs might achieve $\sim 10^{10-11}$ G. Such magnetic fields at centre can be further amplified by the compression during the WD collapse and subsequently by several other possible processes such as the magnetorotational instability (Balbus & Hawley 1991) or Tayler–Spruit dynamo (e.g. Spruit 2002; Reboul-Salze et al. 2024), as well as by simple rotational winding. Consequently, strong magnetic fields, whose poloidal component $B_{\rm p}$ reaches the order of $B_{\rm p} \sim 10^{15}$ G, i.e. magnetar (Usov 1992), might be formed in some AIC events. Therefore, AIC has recently been gaining a further attention because of its potential formation path not only to a rapidly rotating NS but also to a magnetar.

Beside such unique compact star formation channels, the properties of AIC, i.e. low ejecta mass with relatively high velocities, may explain some of the intriguing rapidly evolving transients, such as fast blue optical transients (FBOTs: Drout et al. 2014). Indeed, the work of Yu, Li & Dai (2015) presented a potential connection between these rapid transients and the activities of newly formed NSs, or rather magneters, in the aftermath of AIC or binary NS (BNS) mergers. FBOTs are characterized by their fast rise time till their peak luminosities ($t_{\rm peak} \lesssim 10$ d) and by bolometric peak luminosities ranging from $L_{\rm peak} \sim 10^{42}\,{\rm erg\,s^{-1}}$ to $\sim 10^{44}\,{\rm erg\,s^{-1}}$ (Drout et al. 2014; Inserra 2019, and references therein). Among those remarkable features, the fast rise time ($t_{\rm peak} \sim$ a few to several days) can be explained for instance by a small ejecta mass of $M_{\rm ej} \sim 0.1\,{\rm M}_\odot$ and relatively fast ejecta velocity of $v_{\rm ej} \sim 0.1c$ (e.g. Margutti et al. 2019), which is certainly compatible with the typical AIC models. To explain their peak luminosities, we can apply the most standard energy source, namely the radioactive decay of ^{56}Ni, for fainter events with $L_{\rm peak} \sim 10^{42}\,{\rm erg\,s^{-1}}$, assuming ^{56}Ni mass of $0.1\,{\rm M}_\odot$. On the other hand, this energy source can be ruled out in some events exhibiting higher bolometric luminosities $L_{\rm peak} \sim 10^{44}\,{\rm erg\,s^{-1}}$ (e.g. represented for instance by AT 2018cow, Prentice et al. 2018; Smartt et al. 2018), as the required amount of ^{56}Ni is several $M_\odot$, far exceeding the expected ejecta mass of AICs. Furthermore, the post-peak light curves of these rapid transients are rich in variety and not described by a single power low, inferring that their emission mechanisms may not be explained only by a single scenario (Pursiainen et al. 2018). This fact led us to consider alternative central engine models of FBOTs.

In the investigation of the alternative models, we have to pay attention to both the peak luminosity and the post-peak decline features. To account for the former peak luminosities, a rapidly rotating nascent magnetar or a fall back model onto the black hole (BH) are proposed (Yu et al. 2015; Lyutikov & Toonen 2019; Margutti et al. 2019; Pasham et al. 2021), where the latter BH model can be potentially excluded in the context of AIC scenarios, because of the expected low total mass in the system. Therefore the magnetar engine might be more feasible. Previous studies have deduced the required magnetic field strength to explain the peak luminosity of FBOTs ($L_{\rm peak} \sim 10^{43-44}\,{\rm erg\,s^{-1}}$) and reported $\sim 10^{15}$ G (Rest et al. 2018; Lyutikov & Toonen 2019; Margutti et al. 2019), which indeed falls into the typical strengths of magnetars. Furthermore, the energy deposition rate by magnetar spin-down, which follows $\propto t^{-2}$, into nebulae behind the shock are in line with the observed overall timescales of FBOTs (Drout et al. 2014) as modelled in the context of NS mergers by, e.g. Yu, Zhang & Gao (2013). These facts infer that the magnetar model in the context of AICs may explain the emission mechanism of a subclass of rapidly evolving transients. These facts also motivate us to explore detailed AIC scenarios based on state-of-the-art SN simulations including their plausible formation channel to magnetar.

To date, there are several AIC simulations with various physical inputs. Early one-dimensional spherically symmetric (1D) studies (Baron et al. 1987; Woosley & Baron 1992; Fryer et al. 1999) based on a rather simplified neutrino transport and recent ones (Mor, Livne & Piran 2023; Mori et al. 2024) have commonly reported electron capture collapse of WDs and formation of NSs, followed by a shock expansion, except a short-term model in Baron et al. (1987). In multi-D models, AICs were studied with various focuses. The seminal work by Dessart et al. (2006) has reported that the AIC of rotating WDs in 2D axisymmetry results in a weak explosion triggered by neutrino heating. Abdikamalov et al. (2010) focused on the aspect of gravitational wave (GW) emission from collapse of rotating WDs by performing general relativistic simulations with a simplified microphysics. The first 3D study in this context was reported in Longo Micchi, Radice & Chirenti (2023), which conducted fully relativistic 3D simulations, albeit with an M1 grey neutrino transport. They reported loud GW signals associated with non-axisymmetric rotational instabilities and also witnessed explosion, whose diagnostic explosion energies are $\sim 5 \times 10^{50}$ erg for rotating models. Later the same group performed 2D GRMHD simulations with an M1 grey neutrino transport, aiming at the jet formation to account for long gamma-ray bursts and kilonovae facilitated by strong magnetic fields (Cheong et al. 2025). Very recently, Batziou et al. (2024) reported quite long-term AIC models in 2D with a sophisticated multi-energy neutrino transport. They followed the evolution of the system for ~ 7 s after NS formation and discussed impacts of WD rotation on the proton/neutron richness in the ejecta.

In this paper, we report a new result for 3D numerical relativity simulations of AICs with a multi-energy M1 neutrino transport. Our primary focus is on discussing the impacts of non-axisymmetric instabilities on the matter ejection from central proto-NS (PNS), which are significant especially for rapidly rotating models, and also on presenting detailed thermodynamic properties of ejecta based on our up-to-date neutrino transport. Our results are generally consistent with previous studies, except that our 3D models exhibit quantitatively different ejecta profile, especially for electron fraction, in comparison to previous 2D axisymmetric studies. Afterwards, based on our numerical models, we discuss their peculiar GWs, neutrinos, and electromagnetic signals.

The paper is organized as follows. In Section 2, we explain our initial WD models and how they can be constructed. In addition, our radiation-MHD scheme is concisely summarized. The main results are presented in Section 3. Sections 4.1–4.3 are devoted to a discussion about their multi-messenger signals. We summarize our results and discussion in Section 5. Throughout this paper, cgs unit is used and Greek indices run from 0 to 3. c and G are the speed of light and gravitational constant, respectively.

2 NUMERICAL SET-UP

In this section, we first explain the present initial WD models including how we construct them. Afterwards, we briefly describe our numerical code and set-up.

Table 1. Summary of our models. From left to right, the columns represent the model name, the initial ratio of the rotational kinetic energy to the gravitational potential energy β, central density, angular momentum, rest mass, angular velocity along the rotational axis, the value of β at the core bounce, the time t_9 at which the maximum shock radius reaches 10^9 cm, the explosion energy at $t = t_9$, the time at which the simulation is stopped, and final explosion energy.

Model	β_0 (per cent)	$\rho_{c,0}$ ($g\,cm^{-3}$)	J_0 ($10^{49}\,g\,cm^2\,s^{-1}$)	$M_{WD,bar}$ ($M_\odot$)	Ω_0 ($rad\,s^{-1}$)	β_{cb} (per cent)	t_9 (ms)	$E_{exp,9}$ (10^{50} erg)	t_{fin} (ms)	$E_{exp,fin}$ (10^{50} erg)
R1	0.113	10^{10}	1.05	1.73	1.38	0.56	338	2.54	325	1.01
R2	0.217	10^{10}	2.08	1.74	1.91	1.09	302	2.54	354	2.70
R3	0.320	10^{10}	2.98	1.75	2.31	1.35	317	3.37	381	3.63
R6	0.647	10^{10}	5.86	1.76	3.24	3.56	345	3.11	487	4.18
R6oB	0.647	10^{10}	5.86	1.76	3.24	3.56	390	1.76	455	2.78
R6o	0.647	10^{10}	5.86	1.76	3.24	3.56	–	–	247	0.24

2.1 Initial WD models

We perform collapse simulations of rigidly rotating WDs with various rotational parameters, assuming equatorial or octant symmetry. The initial configuration is in hydrostatic equilibrium and can be constructed for a given central rest mass density $\rho_{c,0}$ and ratio of the rotational kinetic energy, T_{rot}, to the gravitational potential energy W, $\beta \equiv |T_{rot}/W|$, together with thermodynamic quantities to close the system (see e.g. Shibata & Sekiguchi 2004). As one of our aims in this study is to discuss electromagnetic counterparts of AICs, in particular the one associated with a magnetar formation, we further adopt one magnetized model (R6oB), albeit assuming an octant symmetry for the sake of saving computational resource.

In this study, we consider relatively massive rotating WDs, intended to assume Oxygen-Neon-Magnesium (ONeMg) WDs, for which the central density becomes so high that gravitational collapse due to the electron capture is triggered, rather than the detonation branch, i.e. the type Ia SN (Nomoto & Kondo 1991). For this purpose, we always employ high central density as $\rho_{c,0} = 10^{10}\,g\,cm^{-3}$. Regarding the initial WD rotational profile, we choose various parameters $\beta_0 \sim 0.1$, 0.2, 0.3, and 0.6 per cent. We note that it is still a matter of debate, how such rapidly rotating massive WDs having $\sim 1.7\,M_\odot$ can be born in astrophysically plausible binary systems (see Yoon & Langer 2005, for more detailed discussion and possible branches to these WDs).

As for the thermodynamic profile, we simply assume constant electron fraction $Y_e(= 0.5)$ and low entropy $s(= 0.8\,k_B\,baryon^{-1})$ structures, because of the lack of plausible thermodynamic profiles of WD and also to avoid numerical difficulties originated from dealing with too low temperature or entropy. This assumption is one of differences in comparison to many of previous AIC models (Dessart et al. 2006; Abdikamalov et al. 2010; Longo Micchi et al. 2023; Batziou et al. 2024), which give the initial parametrized temperature.

For the present study, we use the SFHo nuclear relativistic mean-field equation of state (EOS) of Steiner, Hempel & Fischer (2013), taking into account the electrons/positrons, and photons contributions. Since the original SFHo EOS table covers the density and temperature regions only of $\rho \gtrsim 10^3\,g\,cm^{-3}$ and $T \geq 0.1$ MeV, respectively, we extend the table down to $\rho = 3 \times 10^{-3}\,g\,cm^{-3}$ and $T \sim 10^{-4}$ MeV using the EOS of Timmes & Swesty (2000), in order to evolve the matter ejected towards the low-density region accurately.

Outside the WDs, we initially set up an artificial atmosphere of sufficiently low density. We first define the WD surface $r_{WD}(r, \theta)$ at $\rho = 10\,g\,cm^{-3}$, where (r, θ) are the normal radius and azimuthal angle defined in the spherical-polar coordinates and r_{WD} is in the range of 1900–2600 km. Beyond the surface, we simply assume a power-law distribution for the atmosphere density $\rho_{atom}(r, \theta)$ as follows:

$$\rho_{atom}(r, \theta) = 10 \left(\frac{r_{WD}(r, \theta)}{r} \right)^3 g\,cm^{-3}. \quad (1)$$

In the present study, ρ_{atom} is always larger than $10^{-3}\,g\,cm^{-3}$ because the outer boundaries of the computational domain is located at $\sim 1.5 \times 10^4$ km along each axis. Y_e and entropy per baryon in the atmosphere are set to be identical with the initial stellar matter, i.e. $Y_e = 0.5$ and $s = 0.8\,k_B\,baryon^{-1}$, respectively.

Magnetic fields (**B**) are given through the vector potential **A** as $\mathbf{B} = \nabla \times \mathbf{A}$, with

$$(A_r, A_\theta, A_\phi) = \left(0,\ 0,\ \frac{B_0}{2} \frac{R_0^3}{r^3 + R_0^3} r \sin\theta \right), \quad (2)$$

where B_0 and R_0 represent the magnetic field strength at centre and the size of central sphere with uniform magnetic fields, respectively. (r, θ, ϕ) denote the usual spherical polar coordinates.

Table 1 summarizes the model name, β_0, $\rho_{c,0}$, initial total angular momentum J_0, initial baryonic WD mass $M_{WD,bar}$, initial angular frequency Ω_0, β value at core bounce β_{cb}, post bounce time t_9 when the maximum shock reaches 10^9 cm, diagnostic explosion energy measured at $t = t_9$, final simulation time t_{fin}, and diagnostic explosion energy at $t = t_{fin}$. The model names R1, R2, R3, and R6 approximately represent $\beta_0 \sim 0.1$, 0.2, 0.3, and 0.6 per cent, respectively. To investigate the impacts of non-axisymmetric effects, we simulate additional two octant symmetry models, whose model name contains 'o'. The magnetized model is labelled as R6oB, for which we employ relatively strong initial magnetic field $B_0 = 10^{11}$ G (see, Wickramasinghe & Ferrario 2000; Schmidt et al. 2003; Zhu et al. 2015, for observational and theoretical support for such strong magnetic field).

Fig. 1 presents the initial spatial profiles of the density, mean atomic number $\langle A \rangle$, and binding energy ϵ_{bind} along the equator. Our fastest rotating model R6 has an enlarged equator radius by ~ 30 per cent compared to $\approx 1.92 \times 10^8$ cm for the slowest model R1.

2.2 Radiation GRMHD code

Numerical computations are carried out using our 3D-GR neutrino-radiation code of Kuroda (2021) and Kuroda & Shibata (2024). It solves the Einstein equations based on the BSSN formalism (Shibata & Nakamura 1995; Baumgarte & Shapiro 1999) with a constraint violation propagation prescription in terms of a Z4c formalism (cf. Hilditch et al. 2013, and references therein) by which a local constraint violation can be propagated away. The code is described on a static Cartesian spatial mesh, for which we employ here the same resolution as in Kuroda (2021). The computational domain extends to 1.5×10^4 km from the centre along each axis,

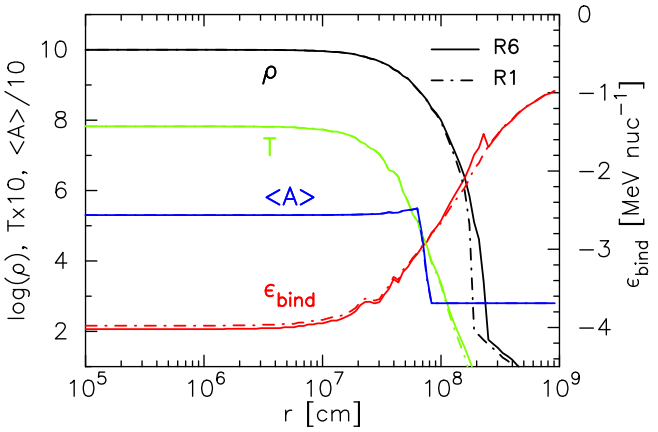

Figure 1. Initial configuration of two representative WD models R1 and R6. Shown are the rest mass density in logarithmic scale $\log(\rho\,[\mathrm{g\,cm^{-3}}])$ (black line), temperature T [MeV] (multiplied by 10; green), mean atomic number $\langle A\rangle$ (multiplied by 1/10; blue), and binding energy $\varepsilon_{\rm bind}$ [MeV nuc^{-1}] (red).

in which 2:1 ratio nested boxes from 0 to $L_{\rm max}$ refinement levels are embedded. In the present study, we set $L_{\rm max} = 11$ and each nested box contains 64^3 cells so that the finest resolution at the centre achieves 229 m. The GR spectral neutrino transport is based on the two-moment scheme with M1 analytical closure (cf. Shibata et al. 2011, and references therein), with the same neutrino energy resolution of 12 bins in the range of 1–300 MeV, as was used in Kuroda (2021). The weak rates used for the collision integral of the neutrino transport equation are given in Kotake et al. (2018).

3 RESULTS

In this section, first, we briefly overview the dynamical evolution of the computed models in Section 3.1. Then in Section 3.2, we describe the ejecta properties in detail.

3.1 Collapse and explosion dynamics

We begin with describing the overall evolution process. As explained in Section 2.1, the inner region of all current WD models are composed of heavy nuclei, and because of the sufficiently high initial central density ($\rho = 10^{10}\,\mathrm{g\,cm^{-3}}$), the electron capture immediately proceeds after the initiation of computation. Consequently, it deprives the electron degeneracy pressure, which is the main force against WD's self-gravity, and induces the gravitational collapse. At ~ 0.13 s after the onset of collapse, all models undergo the core bounce, not by the centrifugal force but by the strong nuclear force, as is evident from the bounce density exceeding a nuclear saturation density $\sim 2\times10^{14}\,\mathrm{g\,cm^{-3}}$. In the meantime, if we switch off the neutrino matter interactions, i.e. in the absence of electron captures, we confirmed that the core does not initiate collapse and stays nearly its initial state at least for 1 s.

There is a slight rotational dependence of the core bounce time on the rotational degree. The fastest rotating models R6/R6o show ~ 1 ms delay in comparison to the slowest one R1. Additionally, the faster rotating model exhibits a lower central density and higher central lapse for a given time as seen in panel (a) of Fig. 2. All these features are general rotational effects and such a trend is preserved throughout the simulation time. The proto-neutron star (PNS) mass also shows a clear rotational dependence in both baryonic $M_{\rm PNS,bar}$

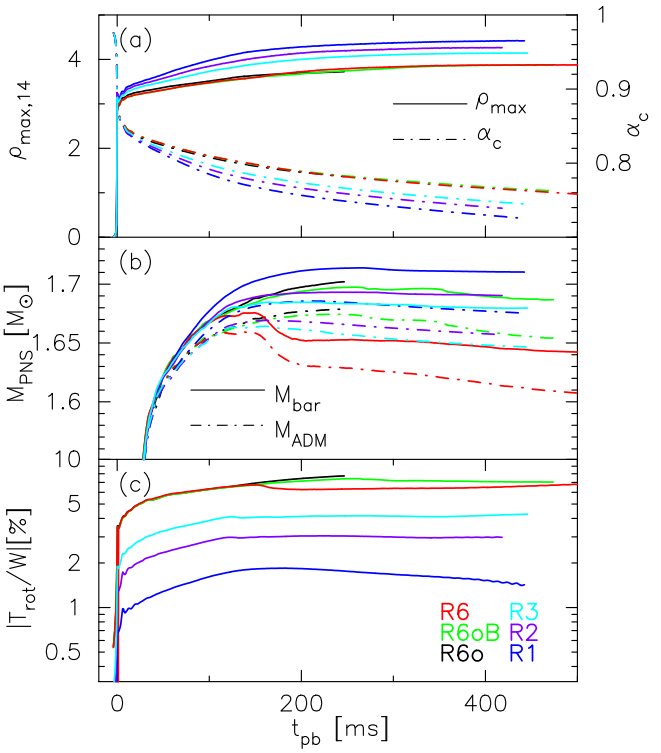

Figure 2. Panel (a): Evolution of the maximum rest mass density $\rho_{\rm max,14}$ (solid) in units of $10^{14}\,\mathrm{g\,cm^{-3}}$ and the central lapse function $\alpha_{\rm c}$ (dash-dotted). (b): The PNS mass in baryonic ($M_{\rm bar}$: solid) and ADM-based value ($M_{\rm ADM}$, see the text for definition: dash-dotted). (c): The ratio of rotational kinetic energy $T_{\rm rot}$ to gravitational potential energy W of PNS.

and Arnowitt–Deser–Misner (ADM)-based mass $M_{\rm PNS,ADM}$[1] (panel b). We define the PNS by the region where the rest mass density exceeds $10^{10}\,\mathrm{g\,cm^{-3}}$. Both $M_{\rm PNS,bar}$ and $M_{\rm PNS,ADM}$ become higher for slowly rotating models. At post bounce times of $t_{\rm pb} \sim 100$–150 ms, the baryonic PNS mass nearly plateaus in models R1, R2, and R3.

At $t_{\rm pb} \sim 100$ ms, the red (R6) and green (R6o) lines start to diverge. While the PNS mass continuously grows in model R6o, a significant decrease is thereafter observed in the counterpart model R6. We will later discuss this noteworthy behaviour. The neutrino emission deprives the internal energy from the PNSs and reduces $M_{\rm PNS,ADM}$ with time, which makes the difference between $M_{\rm PNS,bar}$ and $M_{\rm PNS,ADM}$ gradually larger.

Panel (c) presents the dimensionless rotational parameter $|T_{\rm rot}/W|$. $T_{\rm rot}$ and W here are, respectively, the rotational kinetic and gravitational potential energies of the PNS. From the plot, we see that $|T_{\rm rot}/W|$ in all models exceeds 1 per cent after bounce. In terms of the PNS angular frequency, the frequency goes beyond 1 kHz even in the slowest rotating model R1. One remarkable feature is found in the most rapidly rotating models R6 and R6o and their comparison. Their $|T_{\rm rot}/W|$ reaches ~ 7 per cent at $t_{\rm pb} \sim 150$ ms and then begin to diverge from one another. R6 (red line) exhibits a sudden decrease while the octant symmetry model R6o continues increasing. As mentioned already, the PNS mass in model R6 also shows a similar

[1] See equation 3 in Kuroda & Shibata (2024) for our definition of $M_{\rm PNS,ADM}$. We note that $M_{\rm PNS,ADM}$ is used just as a broad measurement of the gravitational mass of the PNS as it is not yet an isolated system but still surrounded by the original WD envelope, making it difficult to clearly separate the PNS and ejecta.

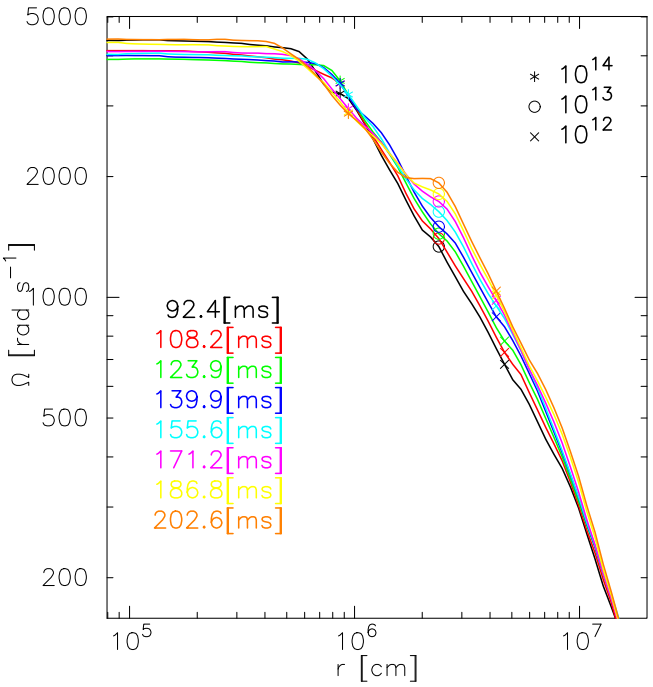

Figure 3. Spatial profile of azimuthal angle averaged angular frequency $\Omega(\varpi)$ for model R6 on the equatorial plane and its time evolution as represented by the post bounce time on the lower-left corner. The radii of angle averaged isodensity surface at $\rho = 10^{12,13,14}\,\mathrm{g\,cm^{-3}}$ are also marked by points shown on the upper-right corner.

sudden decrease at the same time. We attribute these features to the low-$|T_{\rm rot}/W|$ instability (Centrella et al. 2001; Shibata, Karino & Eriguchi 2002, 2003; Ott et al. 2005; Watts, Andersson & Jones 2005; Saijo & Yoshida 2006; Scheidegger et al. 2010; Takiwaki & Kotake 2018). Indeed, such a sudden decrease in $|T_{\rm rot}/W|$ is reported in previous 3D simulations in the context of rapidly rotating neutron star (Ott et al. 2005; Shibagaki et al. 2021). Although a similar mass decrease was not explicitly mentioned in these previous 3D studies, the mass decrease can be naively explained by the formation of strong one-armed spiral waves associated with the low-$|T_{\rm rot}/W|$ instability, which ejects a fraction of gravitationally-loosely bound PNS envelope through the angular momentum transport by the gravitational torque.

The low-$|T_{\rm rot}/W|$ instability is known as an efficient mechanism to redistribute the angular momentum (Saijo & Yoshida 2006). To see whether the observed sudden decrease in both $|T_{\rm rot}/W|$ and $M_{\rm PNS}$ can indeed be attributed to the low-$|T_{\rm rot}/W|$ instability, we examine how the spatial profile of angular frequency evolves across the corresponding period ($100 \le t_{\rm pb} \le 200$ ms). Fig. 3 plots the spatial profile of azimuthal angle averaged angular frequency $\Omega(\varpi)$ for model R6 on the equatorial plane defined by

$$\Omega(\varpi) \equiv \frac{1}{2\pi}\int d\phi \frac{v_\phi}{\varpi}\bigg|_{z=0}, \tag{3}$$

with v_ϕ being the azimuthal component of three-velocity and $\varpi = \sqrt{x^2+y^2}$. We plot several time snapshots in different colours represented by the post bounce time on the lower-left corner. From Fig. 2, we find that $t_{\rm pb} = 92$ and 202 ms correspond to before and after the mass as well as $|T_{\rm rot}/W|$ decrease, respectively. In addition, we overplot the radii of angle averaged isodensity surface at $\rho = 10^{12,13,14}\,\mathrm{g\,cm^{-3}}$ by marks shown on the upper-right corner. These isodensity surfaces will be used later also in our discussion about GW emissions. From the figure, we can clearly see that $\Omega(\varpi)$ drastically increases at $r \sim 25$ km, where the density is $\rho \approx 10^{13}\,\mathrm{g\,cm^{-3}}$, across the corresponding phase. Such a spin-up at an outer region is consistent with the finding of Ott et al. (2005). We simultaneously witness that at a slightly inner region $r \sim 10$ km, a spin-down can be observed. All these features support our interpretation that the low-$|T_{\rm rot}/W|$ instability indeed activates during $100 \le t_{\rm pb} \le 200$ ms and redistributes the angular momentum from inner to outer region, which also works to eject a part of spun-up PNS components and reduces the PNS mass.

Next, we pay attention to the explosion dynamics. Fig. 4 plots the time evolution of the maximum shock radius $R_{\rm s}$ in panel (a), diagnostic explosion energy $E_{\rm exp}$ (b), ejecta mass $M_{\rm ej}$ (c), and ejecta velocity $v_{\rm ej}$ (d). Here, we define the maximum shock radius R_s by the outermost radius where the entropy exceeds $s = 4\,k_{\rm B}\,\mathrm{baryon^{-1}}$. Additionally, $E_{\rm exp}$ and $M_{\rm ej}$ are evaluated by

$$E_{\rm exp} = f_{\rm s}\int_{e_{\rm bind}>0, r>100\,\mathrm{km}} e_{\rm bind}\sqrt{\gamma}\,\mathrm{d}x^3, \tag{4}$$

$$M_{\rm ej} = f_{\rm s}\int_{e_{\rm bind}>0, r>100\,\mathrm{km}} \rho\sqrt{\gamma}\,\mathrm{d}x^3, \tag{5}$$

with the binding energy in each numerical cell $e_{\rm bind}$ being evaluated by (Müller, Janka & Marek 2012b)

$$e_{\rm bind} = \alpha c^2(\tau + \rho\Gamma) - \rho\Gamma c^2. \tag{6}$$

Here, α is the lapse function, τ is the relativistic energy density excluding the rest mass energy (see Kuroda et al. 2020, for the definition), ρ is the rest mass density, Γ is the Lorentz factor, and γ is the determinant of the three-dimensional spatial metric. For the volume integral, we apply additional criterion $r > 100$ km on top of $e_{\rm bind} > 0$ to prevent the matter in the vicinity of the PNS from being identified as unbound. Note that we assume an equatorial and octant symmetry, where we calculate only a domain at $z > 0$ and $(x, y, z) > 0$ of the full 3D domain, respectively. Hence, the factor $f_{\rm s} = 2$ or 8 in equations (4) and (5) is added, which stems from the assumed equatorial or octant symmetry, to account for the contribution from outside the computational domain. Furthermore, from $E_{\rm exp}$ and $M_{\rm ej}$, we approximately estimate the bulk velocity of ejecta $v_{\rm ej}$ as follows:

$$v_{\rm ej} = \sqrt{\frac{2E_{\rm exp}}{M_{\rm ej}}}. \tag{7}$$

The maximum shock evolution indicates that the bounce shock directly leads to the runaway explosion shock wave in all models. At initial post bounce phase of $t_{\rm pb} \lesssim 150$ ms, the faster rotating models show more extended shock positions, i.e. model R6 shows the largest shock radii. This results simply from the enhanced centrifugal force, which drives the shock front further out. During the initial post bounce phase of $t_{\rm pb} \lesssim 150$ ms, however, the more extended shock position implies neither more energetic explosions nor more unbound matters. Indeed, models R1, R2, and R3 show larger unbound mass and diagnostic explosion energy than those of R6 at $t_{\rm pb} \lesssim 150$ ms. A drastic increase in the explosion energy continues till $t_{\rm pb} \sim 200$ ms in all models (middle panel). Thereafter the increase becomes slightly milder. For $t_{\rm pb} \gtrsim 200$ ms, their values settle to a few times of 0.1 B(Bethe $\equiv 10^{51}$ erg). The ejecta mass $M_{\rm ej}$ broadly follows a similar evolutionary path to $E_{\rm exp}$. For $t_{\rm pb} \gtrsim 200$ ms, $M_{\rm ej}$ has in general a correlation with the WD rotation, and models R1 and R6 exhibit the smallest ($M_{\rm ej} \sim 0.02\,\mathrm{M_\odot}$) and largest ($\sim 0.1\,\mathrm{M_\odot}$) mass ejection, respectively. This correlation indicates that the bulk ejecta velocity is always $\sim 0.1\,c$ regardless of the ejecta mass.

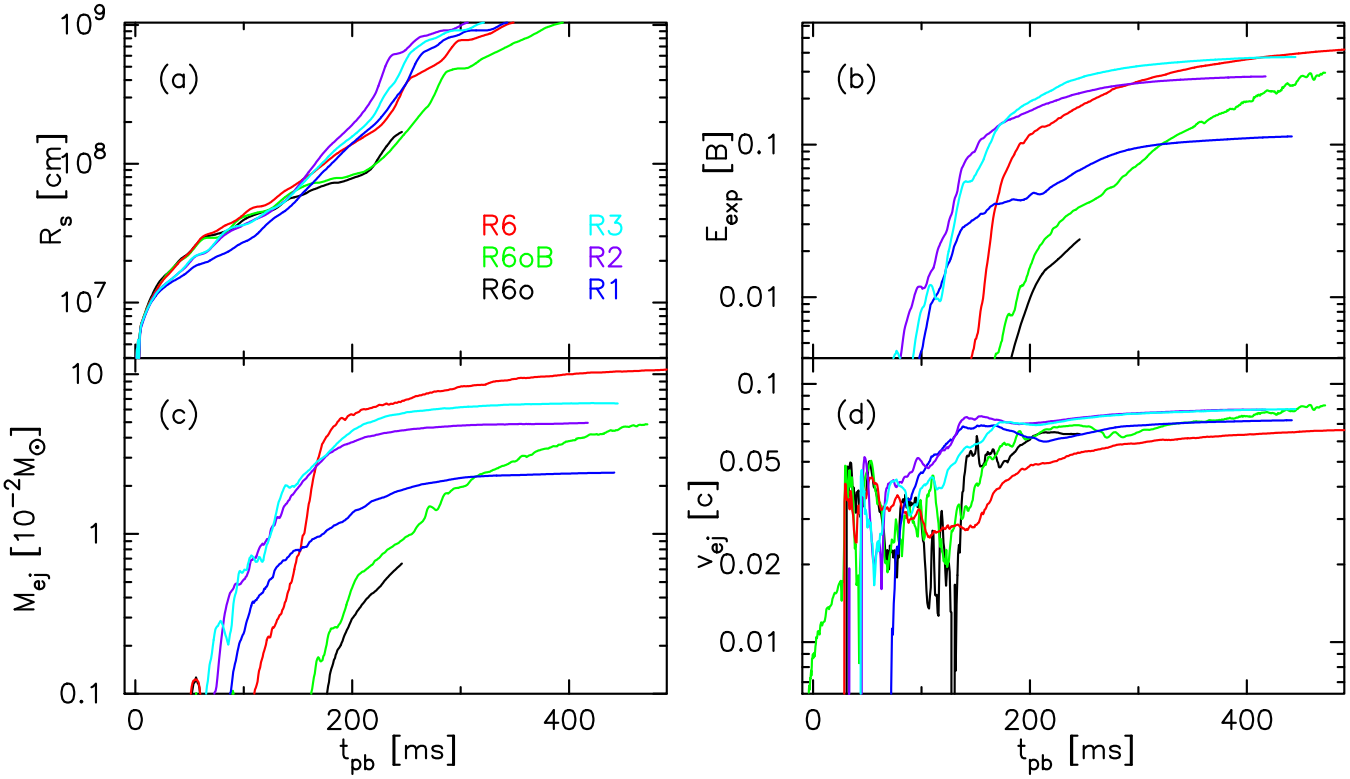

Figure 4. Evolution of the maximum shock radius r_{shock} (top-left), diagnostic explosion energy E_{exp} (top-right), ejecta mass M_{ej} (bottom-left), and bulk velocity of ejecta v_{ej} (bottom-right) for all models.

The magnetized model R6oB indicates a rather similar evolution process with its counterpart non-magnetized model R6o at least during our simulation time of R6o ($t_{pb} \sim 250$ ms). Except a slightly energetic explosion in R6oB, i.e. higher E_{exp} and larger M_{ej}, all behaviours shown in Fig. 4 are quantitatively similar between R6oB (green lines) and R6o (black). Indeed for R6oB we do not observe an emergence of 'magnetically driven jet', inside which the magnetic pressure dominates over the gas pressure typically by 1–2 orders of magnitude larger (e.g. Bugli et al. 2020; Obergaulinger & Aloy 2020; Kuroda & Shibata 2024). In these previous SN models, the initial magnetic field imposed is often one order of magnitude stronger ($\sim 10^{12}$ G) than the value chosen in this work, which results in the magnetically driven jet formation relatively soon after core bounce at $t_{pb} \lesssim 100$ ms. By contrast in model R6oB, the gas pressure always dominates over the magnetic one by approximately one order of magnitude inside the bipolar outflow. This is because the initial poloidal magnetic fields $B_0 = 10^{11}$ G, which is motivated by observational and theoretical studies of strongly magnetized WDs (Wickramasinghe & Ferrario 2000; Schmidt et al. 2003; Zhu et al. 2015), cannot be amplified to the dynamically relevant strength by linear amplification mechanisms within such a short time-scale and/or our numerical resolution (e.g. ~ 450 m at just above the PNS surface $r \sim 30$ km) is not sufficient to resolve potential non-linear amplification mechanisms such as MRI (Balbus & Hawley 1991). From these, we conclude that the explosion witnessed in model R6oB is facilitated mainly by the neutrino heating and the overall explosion dynamics is essentially the same with its counterpart non-magnetized model R6o within our limited simulation times ($t_{pb} \leq 500$ ms). This is more or less consistent with recent AIC models with magnetic fields (Cheong et al. 2025), in which they reported no significant difference during the first 500 ms after bounce among the models using initial magnetic fields of 10^{11} G or weaker.

We, however, mention that there are some non-negligible contributions from magnetic fields. For instance, we find regions outside the outflow opening angle (i.e. $30^\circ \lesssim \theta \lesssim 50^\circ$), where the magnetic pressure dominates over the gas pressure by approximately one order of magnitude. Such highly magnetized regions may possibly influence the mass ejection along with the further magnetic field amplifications. Additionally, the remnant is strongly magnetized, achieving poloidal (B_p) and toroidal (B_ϕ) components of $B_p \sim 10^{14-15}$ G and $B_\phi \sim 10^{16}$ G inside PNS, respectively. Such strong magnetic fields together with rapid rotation for formed NSs can indeed be a key ingredient to explain rapidly evolving bright transients as will be discussed in Section 4.3.

Longo Micchi et al. (2023) have recently performed 3DGR AIC simulations, albeit with a rather simplified neutrino transport and shorter simulations times ($t_{pb} \lesssim 160$ ms) than ours. Their explosion energy and ejecta mass reach ~ 1 B and $\sim 3 \times 10^{-2}\, M_\odot$ in rotating models, while these values remain essentially zero in non-rotating model, i.e. no explosion. Another latest 2D long-time simulations by Batziou et al. (2024) show $E_{exp} \sim 0.01$–0.25 B and $M_{ej} \sim 0.2$–$5 \times 10^{-2}\, M_\odot$ at $t_{pb} \gtrsim 4$ s, which are evaluated at quite a later phase than ours. Admitting that there are several differences in numerical methods and initial WD models between ours and theirs, such as mass and rotational profiles, if we simply compare our explosion energies and ejecta masses with these previous studies, they broadly show a good agreement except our rapidly rotating model R6, which exhibits a considerably larger ejecta mass, $M_{ej} \sim 0.1\, M_\odot$.

The exceptionally large ejecta mass for model R6 can be attributed to the low-$|T_{rot}/W|$ instability. When the low-$|T_{rot}/W|$ instability sets in at $t_{pb} \sim 150$ ms (see the red line in panel c of Fig. 2), the

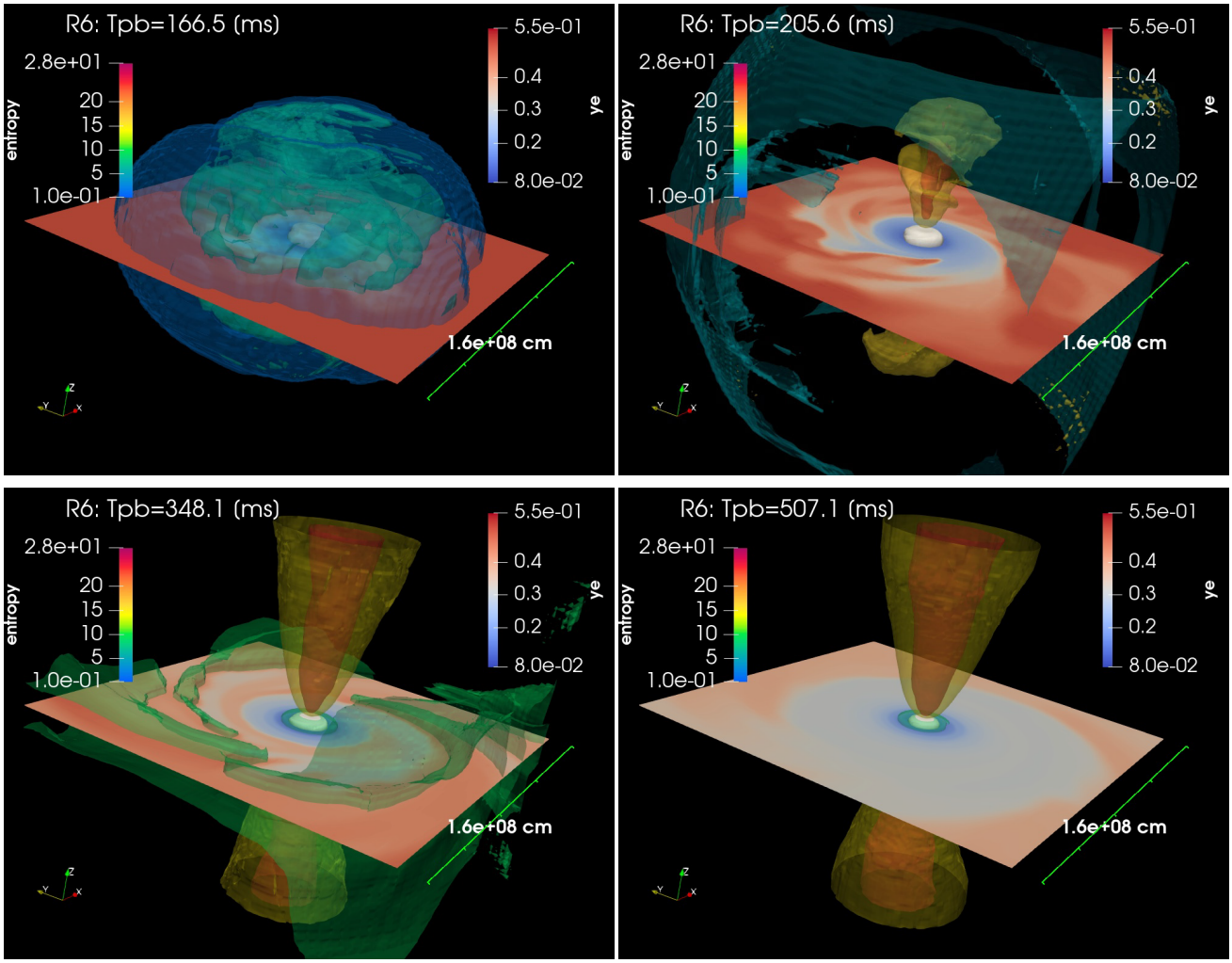

Figure 5. The isoentropy surface and Y_e contour for model R6 within $\sim$ 800 km from the centre. We depict them for four different post bounce times $t_{\rm pb} = 166$ (top-left), 205 (top-right), 348 (bottom-left), and 507 ms (bottom-right). Regarding the Y_e contour, we show its slice on the equatorial plane.

one-armed spiral wave appears and ejects matters, which rapidly increases the unbound mass as can be seen from the red line in the right panel of Fig. 4. Indeed, its counterpart octant symmetry model R6o (black line) exhibits approximately an order of magnitude smaller ejecta-mass evolution, albeit from its limited post bounce evolution, since the octant symmetry completely suppresses the odd-mode non-axisymmetric flow motions including the low-$|T_{\rm rot}/W|$ instability.

From $E_{\rm exp}$ and $M_{\rm ej}$, we approximately measure the bulk ejecta velocity $v_{\rm ej}$ (panel d). As can be seen, all ejecta velocities asymptotically approach $v_{\rm ej} \approx 0.08$ c. Non-magnetized models, especially R2 and R3, exhibit nearly stagnated velocity evolution at $t_{\rm pb} \gtrsim 300$ ms. Regarding $v_{\rm ej}$ in magnetized case R6oB, it is still growing at the final simulation time, which might be due to the aforementioned non-negligible contributions from magnetic fields.

To visualize more clearly the global explosion morphology in model R6, in particular its one-armed spiral structure, we depict the isoentropy surface and Y_e contour at four different post bounce times in Fig. 5. Regarding the Y_e contour, we show its slice on the equatorial plane. At $t_{\rm pb} \sim 166$ ms (top-left), approximately when the low-$|T_{\rm rot}/W|$ sets in, the shock front (outermost bluish surface) shows an oblate structure because of the centrifugal expansion. At $t_{\rm pb} \sim 205$ ms (top-right), we can clearly see fully developed one armed spiral patterns on the equator. Furthermore, the bipolar outflows driven by the neutrino heating also start to emanate. This is because the neutrino luminosity and energy are higher near the rotational axis due to the rotational flattening of the neutrino sphere and increase the heating efficiency there. This is a commonly observed feature in rotating NSs (Summa et al. 2018; Kuroda et al. 2020; Obergaulinger & Aloy 2021; Takiwaki, Kotake & Foglizzo 2021). The bipolar outflow remains at least till the final simulation time of $t_{\rm pb} \sim 500$ ms in model R6. Although not shown, all the rest of our rotating models R1–R3 also exhibit a bipolar structure.

From the final time snapshot (bottom-right), we observe that the low-Y_e(~ 0.3) matters (whitish region) occupy a large domain on the equator ($r \lesssim 800$ km). Longo Micchi et al. (2023) reported that the low-Y_e material ($Y_e \lesssim 0.3$) is confined only to the central region $r \lesssim 200$ km in rotating models at their final simulation time of $t_{\rm pb} \sim$ 150 ms. At a similar post bounce phase ($t_{\rm pb} \sim 166$ ms), our rotating model shows a consistent Y_e distribution with Longo Micchi et al. (2023), with those low-Y_e components being confined to $r \lesssim 200$–300 km. However, our longer time simulations reveal that such low-Y_e components can potentially be ejected at a later phase along with the development of spiral waves originated from the rotational instability.

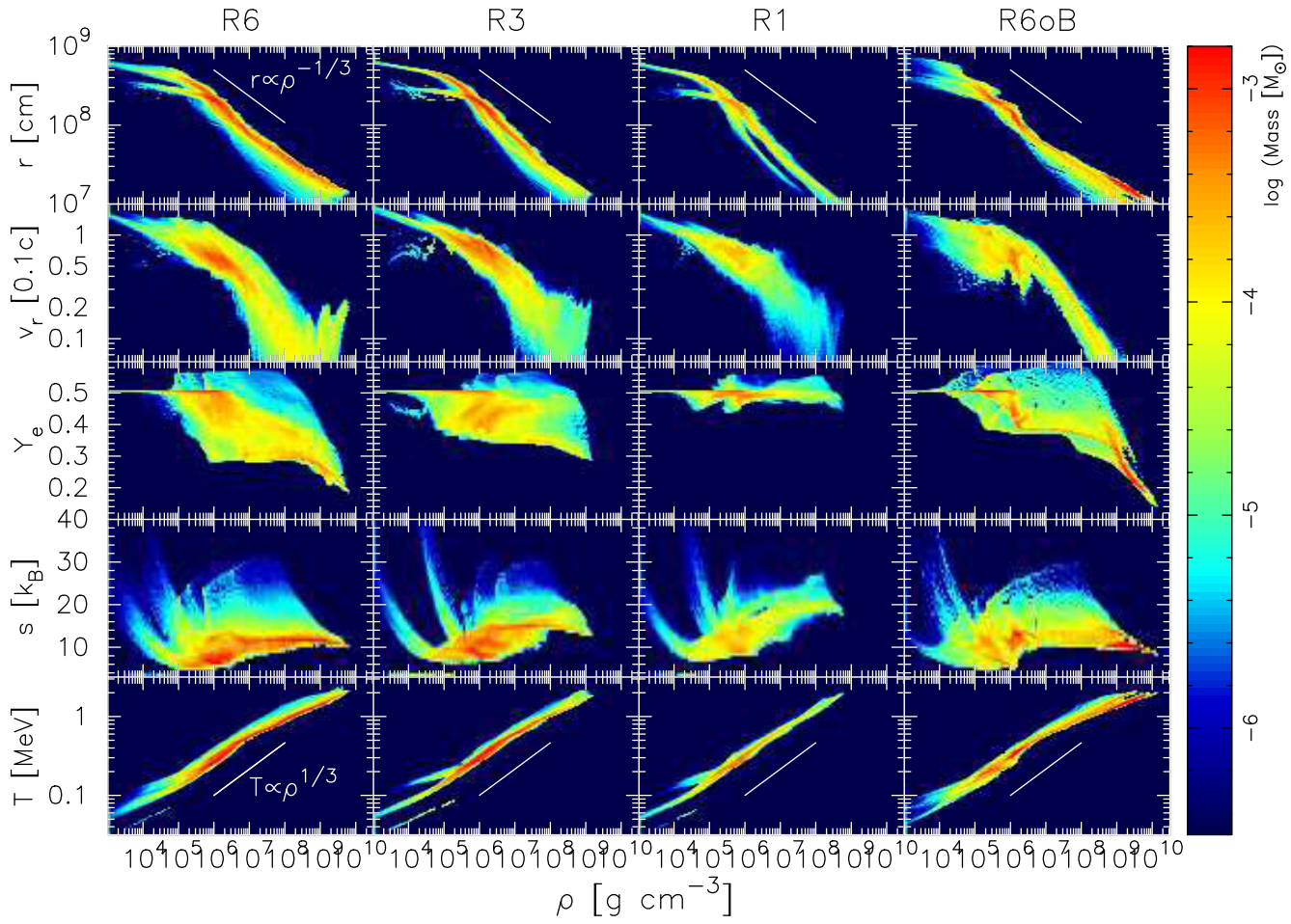

Figure 6. Distributions of unbound fluid elements at the final simulation time on the plane of the rest mass density ρ against (from top) the distance r of ejecta from the centre, radial velocity v_r [0.1c], Y_e, entropy s [k_B baryon^{-1}], and temperature T [MeV]. The colour denotes the integrated mass in units of solar mass in logarithmic scale. For reference, we also add two white lines in the top and bottom panels, denoting the adiabatic relation $T \propto \rho^{1/3} \propto r^{-1}$. Note that we exhibit all ejecta profiles regardless of their expanding direction.

Meantime, we observe high-Y_e components ($\gtrsim 0.55$) concentrating near the rotational axis (will be explained in the next Section 3.2). This is a consequence of relatively high neutrino luminosity and energy near the rotational axis, which increases the efficiency of neutrino absorption and the Y_e value. This feature is also consistent with other 2D AIC models accompanying a bipolar-structure (Dessart et al. 2006; Batziou et al. 2024).

3.2 Ejecta properties

Next, we discuss the ejecta properties. In Fig. 6, we display distributions of unbound fluid elements on the plane of the rest mass density (x-axis) versus: (from top) the distance r of ejecta from the centre, radial velocity v_r [0.1c], Y_e, entropy s [k_B baryon^{-1}], and temperature T [MeV]. We note again that the ejecta are defined by the unbound material locating for $r \geq 100$ km (based on equation 5). The colour denotes the integrated mass in units of solar mass in logarithmic scale. These distributions are evaluated when the maximum shock radius reaches 10^4 km, which corresponds to $t_{pb}(= t_9) = 338$, 317, 345, and 390 ms for models R1, R3, R6, and R6oB, respectively (see Table 1).

The middle raw of Fig. 6 illustrates the Y_e distribution. The most noteworthy impact of rotation is the ejection of a more neutron rich matter with the increase of the initial rotation. This trend can be easily read from the significant amounts of neutron rich ejecta with $0.2 \lesssim Y_e \lesssim 0.4$ for model R6, while those with only $Y_e \gtrsim 0.45$ are ejected for model R1. Albeit an octant symmetric model, another fastest rotating model R6oB also presents a similar profile to that of non-axisymmetric counterpart model R6. We will discuss the difference between R6 and R6oB later. As explained in Fig. 5, these low-Y_e ejecta are the outcomes of faster rotation and associated spiral waves, which dredge up the low-Y_e components initially floating in the envelope of rapidly rotating oblate PNS. At the same time, the initial WD components having $Y_e = 0.5$ and initially locating near the WD surface are another major ejecta, which are expelled from its bottom simply along with the explosion without significantly changing their initial Y_e values.

We observe higher entropy ejecta for slower rotating models. For instance, at $\rho \gtrsim 10^7$ g cm^{-3}, the dominant ejecta appear at $s \sim 20\,k_B$ baryon^{-1} for model R1, which decreases to $s \sim 14$ and $10\,k_B$ baryon^{-1} for models R3 and R6, respectively. In general, the stellar rotation tends to decrease the neutrino luminosity and mean energy. This results in the lower entropy of neutrino heated ejecta (Summa et al. 2018; Kuroda et al. 2020).

From the lower edge of the Y_e distribution, we can infer how the ejecta change their Y_e values along with the ejection. For

instance for model R6, a part of ejecta initially locates at $(\rho, Y_e) \sim (10^{10}\,\mathrm{g/cm^3}, 0.2)$, or in terms of initial location at $r \sim 10^7$ cm (top panel). Note that these values correspond to those near the surface of the PNS. These ejecta are afterwards expelled by the centrifugal force, approximately preserving the Y_e values, or by the neutrino heating, which changes the Y_e values. The increase of Y_e lasts till the neutrino-matter interaction practically ceases at $\rho \sim 10^{8-9}\,\mathrm{g\,cm^{-3}}$. Thereafter, the lower edge of Y_e remains essentially constant and propagates horizontally leftward on this (ρ, Y_e) plane. Because of the different degrees of rotation, which can potentially change the initial location and thermodynamic properties of marginally bound matters, the lower edge of constant Y_e evolutionary path can differ from model to model. Moreover the horizontal, highly populated region in the (ρ, s)-plane below $\rho \sim 10^{8-9}\,\mathrm{g\,cm^{-3}}$ (e.g. the red region in the second panel from bottom for model R6) also indicates the cease of active neutrino-matter interactions, which lets the subsequent thermodynamic evolution nearly adiabatic. Such features are commonly seen also for other models R1–R3.

As has been mentioned, the magnetized model R6oB can be considered as essentially a non-magnetized model during our simulation time ($t_{\rm pb} \lesssim 500$ ms), other than the formation of a strongly magnetized PNS, i.e. magnetar. Therefore, the overall feature of ejecta properties are more or less similar between R6oB and R6 as presented in Fig. 6. However, we can still find non-negligible differences. For instance, the Y_e distribution extends to a slightly lower side $Y_e \approx 0.14$ for model R6oB than $Y_e \approx 0.18$ for R6. Having admitted that longer time simulation is certainly essential to assess whether these lowest-Y_e components can be eventually ejected, as they still locate near the PNS ($r \sim 100$ km, from top panel), they are quite loosely unbound. As they are spatially concentrated at an off-axis region $\theta \sim 40^\circ$, where the magnetic pressure dominates over the gas pressure as mentioned previously, we still cannot exclude possibilities of ejection of such low-Y_e components by magnetic field activities at a later phase. In addition, mass ejection via electromagnetic forces generally suppress the increase of Y_e in comparison to the neutrino heating process, which might result in more visible impacts of magnetic fields on lowering the final Y_e distribution. To clarify the final properties of the ejecta, it is necessary to study the magnetized model with the longer-term evolution.

The velocity distribution shows that most of ejecta are driven outward at the velocity of ~ 0.01–0.1 c, which is consistent with the estimated bulk velocity in Fig. 4. The most rapidly rotating model R6 exhibits a broader velocity distribution ($0.01\,\mathrm{c} \lesssim v_r \lesssim 0.1\,\mathrm{c}$), while R1 shows a slightly narrower profile ($0.05\,\mathrm{c} \lesssim v_r \lesssim 0.1\,\mathrm{c}$). From a comparison between models R6 and R6oB, we observe a similar profile among them. Namely, R6oB also presents a velocity distribution composed of slow ($\sim 0.01\,c$) and fast ($\gtrsim 0.1\,c$) ejecta, which is distinct from that of R1. Temperatures inside ejecta, which have already been accelerated beyond $v_r \gtrsim 0.05$ c, decrease below $T \lesssim 0.3$ MeV due to adiabatic cooling. Indeed the temperature and rest-mass density approximately satisfy the relation $T \propto \rho^{1/3} \propto r^{-1}$ as can be seen from the two white reference lines in the top and bottom panels, indicating that the ejecta expand approximately adiabatically. A fraction of these ejecta have relatively low Y_e of ~ 0.3, which would be of interest from the perspective of nucleosynthesis. As a comparison with recent 3D study of Longo Micchi et al. (2023, see their fig. 22), we generally observe more scattered distributions, e.g. higher velocities, lower temperatures, and both higher- and lower-Y_e matters. Beside a difference in the neutrino transport between ours (multi-energy) and theirs (grey single-energy), those differences seen in the distribution can be attributed to our longer simulation times. The longer-term simulations simply enable us to follow a later phase of the aforementioned nearly adiabatic expansion of ejecta, which generally extends the temperature distribution towards a lower side, and also unbind more matters, which are otherwise still unbound if the simulation time is shorter, by neutrino heating or angular momentum transfer associated with the non-axisymmetric instability, leading to the ejection of both lower- and higher-Y_e components. Recent long-term models of Batziou et al. (2024) also report scattered distributions.

We also find that the radial distribution (top-row) is sometimes not aligned along a single line. This can simply be attributed to the multicomponent nature of explosion morphology. For instance, there is an outflow structure along the pole and at the same time an expanding structure is observed towards equator. Therefore, the ejecta having a same density sometimes appear at different locations (or radii) among these distinct explosion components.

In Fig. 7, we show the spatial profile of ejecta Y_e on the xz- (top panels) and xy-plane (bottom panels) for four selected models R6, R3, R1, and R6oB at $t_{\rm pb} = t_9$. As already explained, strong spiral waves emanate for model R6, which efficiently transport low-Y_e component from the centre to outer envelope. This can be seen in the bottom-left panel. Such a spiral feature becomes less prominent with the decrease of rotation and is naturally absent in the octant symmetry model R6oB. As for another remarkable impact of rotation, the central low electron fraction region itself, e.g. the dark blue region having $Y_e \lesssim 0.2$, is obviously more extended for model R6 and R6oB than the slower rotating models due to the centrifugal force. This property also makes the low-Y_e matters, which initially rotate in the vicinity of PNS surface, e.g. at around the edge of central blue region, more easily ejected simply due to their weaker gravitational bound. On the xz-plane, the Y_e distribution exhibits a stronger angle dependence for more rapidly rotating models. For instance within the outflows ($\theta \lesssim 15^\circ$) for model R6, high-Y_e(~ 0.55) matters are the main components, which are surrounded by rather lower electron fraction outflows with $Y_e \lesssim 0.3$ along the diagonal direction. Such an angular distribution is consistent with previous studies (Dessart et al. 2006; Batziou et al. 2024; Cheong et al. 2025). If the initial rotation becomes slower, such features become more moderate and the overall structure approaches more spherically symmetric as can be seen in R1. From a comparison between R6 and R6oB, the profile on xz-plane is more or less similar. We find a clear bipolar structure, which is surrounded by low-Y_e components (yellowish region). On the whole equatorial plane in R6oB, we find that high-Y_e materials are evidently covering the region, which is a consequence of the absence of spiral waves and is a noticeable difference from the structure seen in the model R6.

To quantitatively discuss the ejecta properties with respect to the WD rotation, we plot the Y_e mass distribution of ejecta for all models in Fig. 8. The vertical axis denotes the integrated mass in each Y_e bin. Since our simulation time is quite limited ($t_{\rm pb} \leq 500$ ms), we plot two distributions applying $r > 10^7$ or $> 2 \times 10^8$ cm criterion when evaluating the histogram; the thick and thin lines denote the Y_e histogram for unbound materials beyond $r > 10^7$ and 2×10^8 cm, respectively. We assume that the ejecta which have been already driven away beyond $r > 2 \times 10^8$ cm, i.e. approximately corresponding to the initial WD radii (see Fig. 1) could hardly fall back again on to the central PNS and would thus be safely ejected.

As a general feature, the WD rotation broadens the spectrum. We indeed observe significantly larger ejecta masses at both the lower- and higher-Y_e sides for models R6 and R6oB compared to those for slower rotating models. In particular, the prolongation of lower side is more sensitive to the rotation. Batziou et al. (2024) have also presented that, for a given WD mass, the Y_e distribution

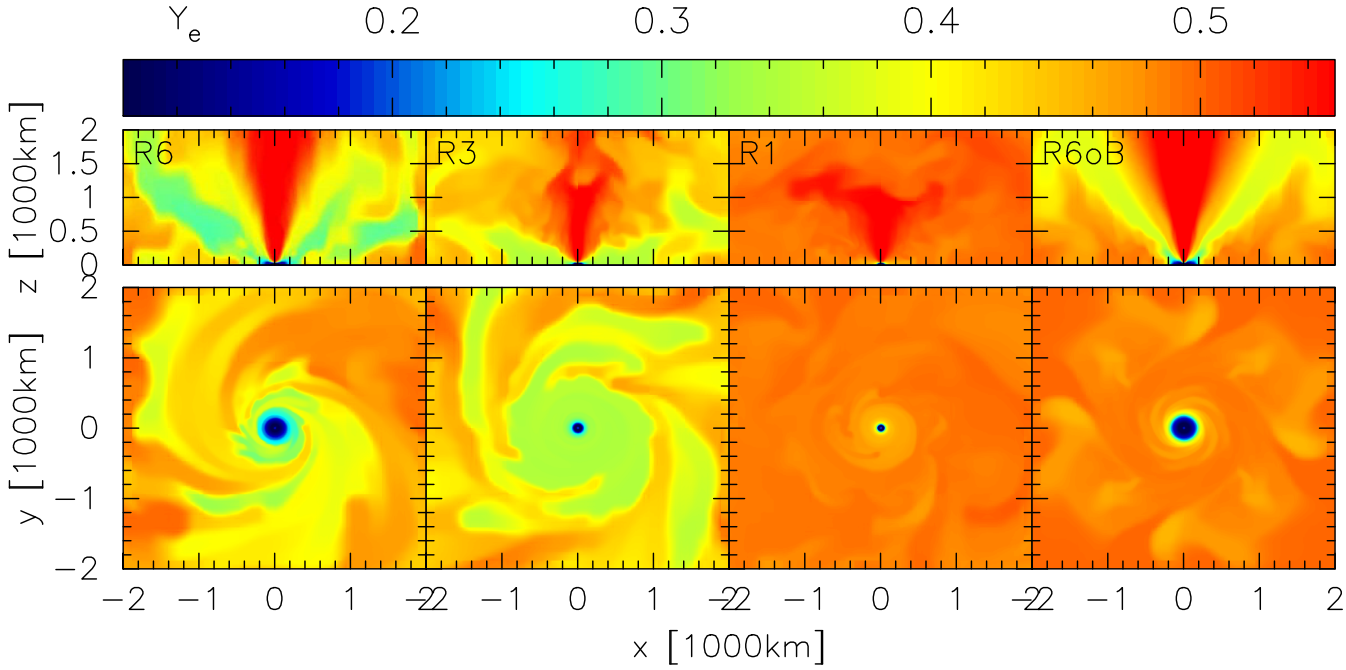

Figure 7. Distributions of electron fraction Y_e on the xz-plane (top panels) and xy-plane (bottom panels), for four selected models R6, R3, R1, and R6oB at $t = t_9$.

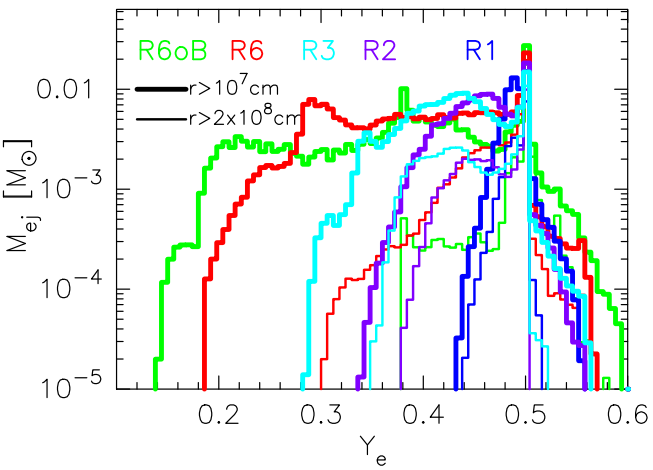

Figure 8. Mass histograms as a function of the electron fraction Y_e for all models. The histograms are evaluated when the maximum shock radius reaches $R_s = 10^9$ cm. The thick and thin lines denote the ejecta locating at $r \geq 10^7$ and $\geq 2 \times 10^8$ cm, respectively.

becomes broader for more rapidly rotating models. From the red thin line, AICs of rapidly rotating WDs, like R6, would reasonably eject low-Y_e components down to 0.3. We find even lower-Y_e unbound materials with $0.2 \leq Y_e \leq 0.3$ as indicated by the red thick line, i.e. spatially locating between $r = 10^7$ and 2×10^8 cm. However, we expect that their Y_e values would increase afterwards, as they are still subject to be exposed to intense neutrino radiation till they reach far enough from the PNS. Consequently their Y_e distribution concentrates at $Y_e \sim 0.28$ as can be seen by a small peak in the thick red line. The rest-mass density of such ejecta with $Y_e = 0.28$ has already been decreased below 10^{8-9} g cm^{-3} as explained in Fig. 6, which is sufficiently low to cease the neutrino–matter interactions and to subsequently preserve their Y_e values. We can therefore reasonably estimate the final ejecta mass with $Y_e \sim 0.3$ to be $\sim 0.01\,M_\odot$. According to previous nucleosynthesis calculations (in a different context, e.g. Fujibayashi et al. 2023), ejecta with $Y_e = 0.3$ might produce elements up to the second r-process peak (mass numbers $A \sim 130$), which should be confirmed by our future long-term AIC simulations. As demonstrated in Batziou et al. (2024), some low-Y_e materials with $Y_e = 0.3$ which exist in the vicinity of PNSs could be eventually ejected beyond WD surface at a quite later phase ($t_{pb} \gtrsim 2$ s). This may partially support our statement above.

On proton-rich side $Y_e > 0.5$, we observe another broadening effect by rotation. These proton-rich ejecta are concentrated along the rotation axis as indicated in the upper panels of Fig. 7. This distribution is explained in the following manner. Near the rotation axis, a neutrino sphere is formed at smaller radii and thus a higher temperature region is formed along the rotation axis compared to that on equator. This leads to more intense neutrino irradiation with higher emergent neutrino energy and efficiently heats matters, increasing their Y_e values near the rotation axis as reported in previous rotating SN simulations (Summa et al. 2018; Kuroda et al. 2020; Obergaulinger & Aloy 2021; Takiwaki et al. 2021). However, we note that there is a caveat that an elongated dumbbell-shaped neutrino sphere due to rapid rotation may artificially increase the efficiency of neutrino absorption for the current M1 neutrino transport as discussed in Just et al. (2015, and references therein).

Before closing this section, we explain the difference seen in the ejecta properties between non-magnetized model R6 and magnetized one R6oB. In Fig. 6 and also from thick red (R6) and green (R6oB) lines in Fig. 8, we may apparently interpret that the magnetized model R6oB eject neutron-richer materials ($Y_e \leq 0.2$) than R6 does. However, those low-Y_e materials for model R6oB are still locating in the vicinity of the central PNS surface ($r \sim 100$ km, from Fig. 6). In the presence of magnetic fields, these low-Y_e materials tend to be defined as unbound according to our current criterion, equation (4), because of the additional contribution from magnetic energy,

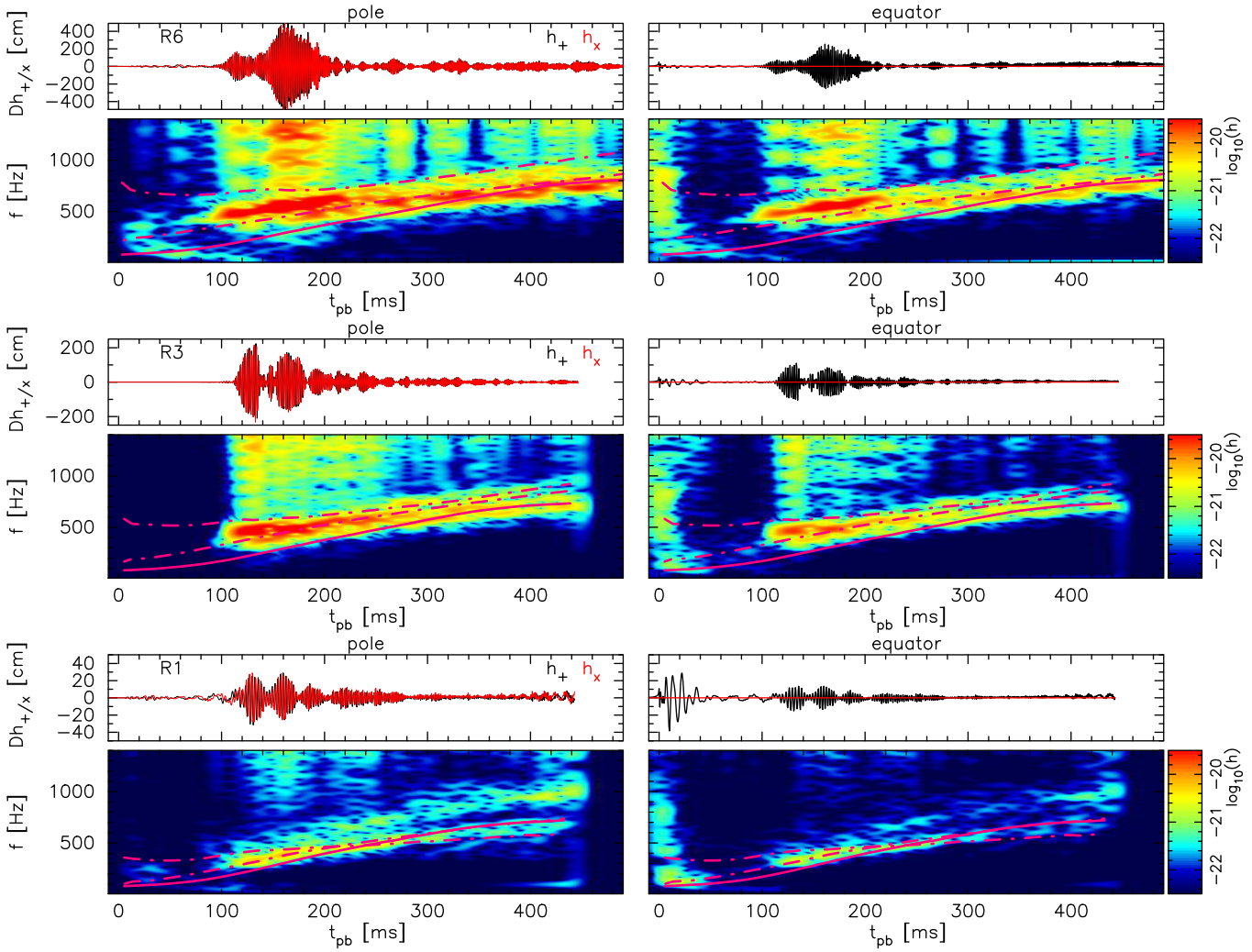

Figure 9. GW strains multiplied by the source distance D for plus (h_+: black solid lines) and cross ($h_\times$: red lines) modes and spectrograms of their characteristic strains for model R6 seen along the pole (left-hand panels) and the equator (right-hand panels) assuming a source distance of 10 kpc. Note that because of the assumed equator symmetry, $h_\times$ along the equator (red line in the top-right panel) completely vanishes. In the spectral evolution, we overplot the analytical prediction for the peak frequency of g-mode oscillations $f_{\rm peak}$ (Müller et al. 2013) by the solid line and two angular frequency evolution curves by the dash–dotted lines (see the text for their definition). We change the colour of the overplotted lines just for the visualization.

in particular when they locate at a region where the local magnetic energy is quite large, as is the current case. If we compare ejecta-Y_e values measured at a sufficiently distant region (thin lines in Fig. 8), we notice that model R6 (thin red line) presents slightly neutron-richer ejecta than R6oB (thin green line). From these, we interpret that the non-axisymmetric instabilities are the primary factor among the suite of current numerical set-ups that eject low-Y_e components to outer region. At the same time, we still cannot dismiss the contribution of strong magnetic fields, which certainly decreases the gravitational binding energy of a part of PNS envelope and may facilitate the mass ejection. We should also add that if we artificially employ stronger magnetic fields, for instance $B_0 = 10^{12}$ G as done in Cheong et al. (2025), the magnetically driven jets may generally eject lower-Y_e components before the ejecta capture a large amount of neutrinos and increase their Y_e. In the meantime, one should pay attention to the compatibility of such strong initial magnetic fields with the values obtained from WD observations and evolution models (Wickramasinghe & Ferrario 2000; Schmidt et al. 2003; Zhu et al. 2015).

4 MULTIMESSENGER SIGNALS

In this section, we discuss observable multimessenger signals from AICs: GWs, neutrinos, and electromagnetic counterparts.

4.1 Gravitational wave emissions

First we discuss the GW signal. Fig. 9 exhibits $Dh_{+/\times}$ (upper panels) and colour-coded spectrograms of $|h|$ in logarithmic scale (lower panels), where D and $h_{+/\times}$ are the source distance and GW strain with two polarized modes $+/\times$. The left and right column are for an observer along the pole and equator (this time, x-axis), respectively. From the top to bottom rows, we display the results for models R6, R3, and R1. Since R2 shows a consistent trend with the rest of models, we omit its plot this time. Regarding the magnetized model R6oB, we simply remove it from the discussion below, as its assumed octant symmetry makes its GW signals essentially the same with those of axisymmetric case and the discussion including all non- and axisymmetric models is not so straightforward. The

GW strain $h_{+/\times}$ are evaluated from a standard quadrupole formula (Shibata & Sekiguchi 2003; Kuroda, Takiwaki & Kotake 2014). To investigate the spectral evolution of GWs, we evaluate the viewing-angle-dependent characteristic strain for an optimally oriented source (Shibagaki et al. 2021; Takiwaki et al. 2021). In the top panels, two polarized modes are plotted in different colours. As we assume equator ($z = 0$) symmetry, $h_\times$ (red line) is completely suppressed along the equator. In addition in the spectral evolution, we overplot the analytical prediction for the peak frequency of g-mode oscillations $f_{\rm peak}$ (Müller, Janka & Marek 2013) by the solid line and two evolution curves corresponding to the angular frequencies of a rotating object $\omega^n_{\rm rot}$, which is divided by π, i.e. dash–dotted curves plot $\omega^n_{\rm rot}/\pi (\equiv f^n_{\rm rot}$; explained below).

In the original studies of Murphy, Ott & Burrows (2009) and Müller et al. (2013), $f_{\rm peak}$ is introduced to explain the Brunt–Väisälä frequency measured on the neutrino sphere assuming no PNS rotation, which is ultimately translated into the gravitational acceleration and the mean energy of emergent electron antineutrinos (Müller et al. 2013). Therefore, the required quantities to evaluate the gravitational acceleration ($M_{\rm PNS}/R^2_{\rm PNS}$, where $M_{\rm PNS}$ and $R_{\rm PNS}$ refer to the PNS mass and radius, respectively) or emergent neutrino energy are simply applied by spherically averaged values, which is feasible as long as the PNS rotation is significantly slow. Meanwhile the current models are rotating models and have a significant polar angle dependence due to rotational flattening of the core. For instance, the PNS radius $R_{\rm PNS}$, which is in a standard definition the isodensity surface at $\rho \sim 10^{10}\,{\rm g\,cm^{-3}}$, differs significantly between the polar and equator directions, e.g. more than 10 times difference in the most rapidly rotating case R6. Therefore, the normally used spherical averaged values may not make sense this time. We instead measure them along the pole and calculate $f_{\rm peak}$, which can nicely fit the observed spectral feature as exhibited later. If we calculate $f_{\rm peak}$ using the values measured along equator, it becomes approximately a few orders of magnitude smaller.

The angular frequency $\omega^n_{\rm rot}$ broadly measures the mean angular frequency of a *spherical shell*, whose density is in the range from 10^n to $10^{n+1}\,{\rm g\,cm^{-3}}$, and is evaluated by

$$\omega^n_{\rm rot} = J^n_z / I^n_z. \tag{8}$$

Here, J^n_z and I^n_z denote the angular momentum and moment of inertia of a shell with respect to the z-axis and are defined by

$$J^n_z = \int_{10^n<\rho<10^{n+1}\,{\rm g\,cm^{-3}}} {\rm d}V (x^2+y^2) \frac{S_\phi}{\sqrt{x^2+y^2}}, \tag{9}$$

$$I^n_z = \int_{10^n<\rho<10^{n+1}\,{\rm g\,cm^{-3}}} {\rm d}V \rho^* (x^2+y^2). \tag{10}$$

In the above, ${\rm d}V = {\rm d}x^3$, $\rho^* (= \rho W\sqrt{\gamma})$ is a weighted density, and S_ϕ is the azimuthal component of conserved linear momentum of fluid S_i. From a rotating object with an angular frequency $\omega_{\rm rot}$, its characteristic GW frequency $f_{\rm rot}$ becomes (e.g. Maggiore 2007)

$$f_{\rm rot} = 2\left(\frac{\omega_{\rm rot}}{2\pi}\right), \tag{11}$$

where the factor 2 accounts for two GW emissions during one rotation. Therefore, the dash–dotted curves, which present $\omega^n_{\rm rot}/\pi = f^n_{\rm rot}$, correspond to the GW frequency from rotating objects, or shells this time, having certain densities. We plot $f^{13}_{\rm rot}$ and $f^{12}_{\rm rot}$, where $f^{13}_{\rm rot} > f^{12}_{\rm rot}$ during our simulation times for all models.

From Fig. 9, we observe quite loud GW signals for model R6 reaching $Dh \sim 500\,{\rm cm}$ between $t_{\rm pb} \sim 100\,{\rm ms}$ and $\sim 200\,{\rm ms}$, in particular for a polar observer. These signals are also found for other models, but with lower amplitude, $Dh \sim 200\,{\rm cm}$ and 30 cm for models R3 and R1, respectively. From Fig. 2, we can identify that the period, when these signals are emitted, completely overlaps the emergence of strong spiral motions. Previous 3D rotating NS models (Shibata & Sekiguchi 2005; Ott et al. 2007; Scheidegger et al. 2010; Kuroda et al. 2014; Takiwaki & Kotake 2018; Shibagaki et al. 2021) and also recent 3D AIC models (Longo Micchi et al. 2023) have reported such quasi-periodic GW signals with comparable amplitudes. These signals can be attributed to the emission from a rotating ellipsoid. Indeed, the wave amplitudes become nearly half (e.g. $Dh \sim 250\,{\rm cm}$ in R6) for an equator observer, which is consistent with the theoretically expected angle dependence $h_+ \propto (1+\cos^2\theta)/2$ (Maggiore 2007). As already discussed in Fig. 3, the spiral waves coming from the low-$|T_{\rm rot}/W|$ instability redistribute the angular momentum from inner to outer region, and consequently weaken the degree of differential rotation. Since the low-$|T_{\rm rot}/W|$ instability is sustained by strong differential rotation and possibly its associated shear instabilities (Watts et al. 2005), the spiral motion is a transient phenomenon and disappears when the degree of the non-axisymmetric deformation becomes small. Therefore, the associated GWs also subside within a time-scale of $\sim$ 10–100 ms (see also Fig. 3), which are also consistent with previous studies (Shibata & Sekiguchi 2005; Saijo & Yoshida 2006; Ott et al. 2007; Scheidegger et al. 2010; Kuroda et al. 2014; Takiwaki & Kotake 2018; Shibagaki et al. 2021), while there are inevitable differences originated from the different microphysics input and PNS property.

After the cease of the strong GW emissions associated with the non-axisymmetric deformation ($t_{\rm pb} \gtrsim 200\,{\rm ms}$), the GW amplitudes decrease significantly, by approximately a factor of 5, for all models. From the spectral evolution, however, ramp-up features are still continuously observed regardless of the models and the observer angle. For instance for model R6, the feature seems to begin from $f \sim 500\,{\rm Hz}$ at $t_{\rm pb} = 100\,{\rm ms}$, which is most likely associated with the aforementioned spiral motion, to $\sim 800\,{\rm Hz}$ at $t_{\rm pb} = 500\,{\rm ms}$. In general, such ramp-up features may be explained by the g/f-mode oscillations of the *non-rotating* PNS (Morozova, Piro & Valenti 2018; Torres-Forné et al. 2019; Sotani & Takiwaki 2020), which are indeed observed in many of previous SN simulations with non-rotating progenitor stars (Murphy et al. 2009; Müller et al. 2013; Kuroda, Kotake & Takiwaki 2016; Mezzacappa et al. 2020; Vartanyan & Burrows 2020; Shibagaki et al. 2021). However, all models in this study are rotating models with strong spiral waves appearing at $100\,{\rm ms} \lesssim t_{\rm pb} \lesssim 200\,{\rm ms}$. Moreover, the peak frequency range during the emergence of strong spiral waves, for instance $f \sim 500(300)$–$700(500)\,{\rm Hz}$ for model R6 (R1), is significantly higher than the typical values ($f \sim$ 100–200 Hz) of g/f-mode oscillations in the corresponding phase of non-rotating models (Murphy et al. 2009; Müller et al. 2013; Kuroda et al. 2016; Mezzacappa et al. 2020; Vartanyan & Burrows 2020; Shibagaki et al. 2021).

To understand the origin of ramp-up features, which are quantitatively different from typical values from non-rotating models, we compare the spectral feature and three different frequencies $f_{\rm peak}$ (solid line), $f^{12}_{\rm rot}$ (dash–dotted), and $f^{13}_{\rm rot}$ (dash–dotted). During the strong GW emission phase ($100\,{\rm ms} \lesssim t_{\rm pb} \lesssim 200\,{\rm ms}$), it is obvious that the typical g/f-mode frequencies $f_{\rm peak}$ (red solid line) do not match the frequency of background strong features. The disagreement becomes more pronounced with the increase of the rotation. We notice that the two frequency curves $f^{12}_{\rm rot}$ and $f^{13}_{\rm rot}$ associated with the fluid rotation appear to be encompassing those strong signals. This clearly indicates that the initial strong signals are originated from rotating objects, specifically whose density is around $\sim 10^{13}\,{\rm g\,cm^{-3}}$. We note again that one dash–dotted curve $f^n_{\rm rot}$ represents an averaged

rotation frequency of fluids, whose density is in the range of 10^n and 10^{n+1} g cm^{-3}. Our interpretation can be strongly supported by the evolution of angular velocity $\Omega(\varpi)$ in Fig. 3. As explained, the angular momentum redistribution and its consequent spin-up are most visible at a region, where the rest-mass density is about 10^{13} g cm^{-3}. This indicates that the corresponding region is suddenly accelerated and that the non-axisymmetric flow patterns are rapidly developed, leading to the strong GW emissions. From these facts, we conclude that the overall ramp-up feature is consisted of two components: the initial rotational origin and the later g/f-mode origin mode.

We also find GW signals which are typically seen in rotating SNe. The first one is the signal at core bounce, namely the Type I signal (Dimmelmeier, Font & Müller 2002; Dimmelmeier et al. 2008). An observer along the equator would observe burst GW signals, whose amplitude reach $|Dh_+| \sim 55$ cm and 11 cm for models R6 and R1, respectively, which can be translated into $|h_+| \sim 2 \times 10^{-21}$ and 4×10^{-22} assuming a source distance of $D = 10$ kpc. As models R6 and R1 have a rotational parameter at bounce of $\beta_{\rm cb} \approx 3.56$ and 0.56 per cent (see Table 1), our result broadly obeys the universal relation between $\beta_{\rm cb}$ and $|h_+|$ at bounce reported by Dimmelmeier et al. (2002, 2008), and Abdikamalov et al. (2010). Regarding another feature, we witness quasi-monotonically growing GWs, only in h_+ along the equator, in the explosion phase $t_{\rm pb} \gtrsim 200$ ms (see also Fig. 4). These signals are emitted from anisotropic matter outflows as reported in previous rotating massive stellar collapse simulations exhibiting bipolar explosions (Obergaulinger et al. 2006; Shibata et al. 2006; Murphy et al. 2009; Vartanyan & Burrows 2020; Shibagaki et al. 2024). Among the set of our current models, the most rapidly rotating model R6 presents the largest growth rate, as its bipolar structure is most visible. At $t_{\rm pb} \sim 450$ ms, Dh_+ increases to ~ 30 cm for model R6, while it does only to ~ 2 cm for model R1. Particularly for model R6, these *memory* signals imprint their characteristic frequency into the spectral evolution, appearing at low frequencies $f \lesssim 10$ Hz, which is marginally visible in the spectral evolution along the equator at $t_{\rm pb} \gtrsim 300$ ms and at $f \sim 10$ Hz, i.e. the lower edge of the figure, for model R6.

Before closing this subsection, we discuss the detectability of GWs. Fig. 10 plots the detectability of matter origin GWs for models R1, R2, R3, and R6 in different colours. $h_{\rm char}$ is the GW spectral amplitude assuming a source distance of $D = 1$ Mpc. The upper and lower panels are for an observer along the pole and equator, respectively. We overplot the sensitivity curves of the current- and third-generation GW detectors: advanced LIGO (aLIGO), advanced VIRGO (AdV), KAGRA (Abbott et al. 2018); Einstein Telescope (ET) (Hild et al. 2011); and Cosmic Explorer (CE) (Abbott et al. 2017). Model R6 exhibits a strong spectral peak at $f = 561$ Hz, whereas slower rotating models have a weaker peak signal appearing at lower frequencies as $f = 472$ (R3), 443 (R2), and 392 Hz (R1). By comparing the spectral evolution in Fig. 9, these signals peaking at frequencies, $400 \lesssim f \lesssim 560$ Hz, are mainly emitted during the emergence of strong spiral waves at $100 \leq t_{\rm pb} \leq 200$ ms and are thus associated with the non-axisymmetric fluid rotation. Therefore the peak frequency increases with the rotation. As has already explained, these peaks are originated from the spiral waves and therefore the peak is approximately halved for an equatorial observer (lower panel). If we observe rapidly rotating AIC events (e.g. models R6 and R3) along the pole and D is smaller than ~ 1 Mpc, the peak signal can be well detected even by the current generation detectors. Using the third-generation detectors (ET and CE), we will be able to detect the peak signals from rapidly rotating AIC events even for $D \sim 10$ Mpc; we may assume a more realistic event rate. If we

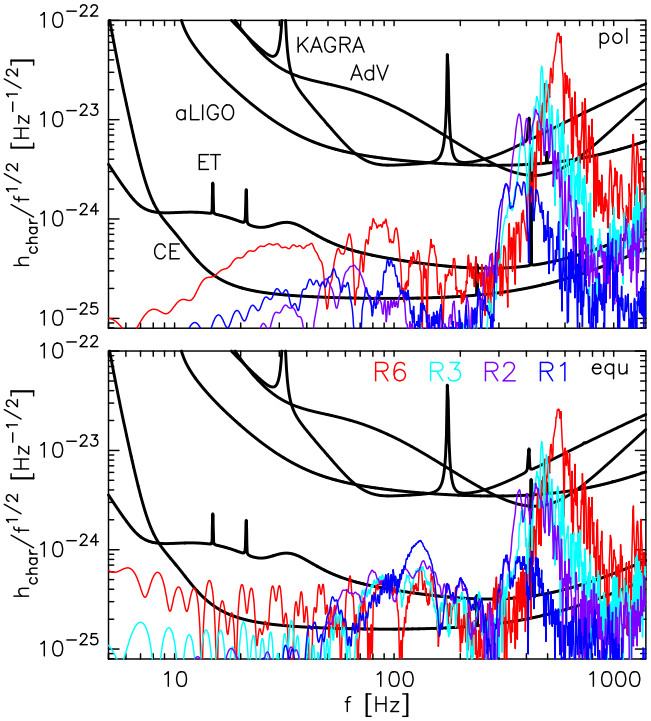

Figure 10. Characteristic strain of matter origin GWs (colour-coded lines) overplotted by the sensitivity curves of the current- and third-generation GW detectors (black): advanced LIGO, advanced VIRGO, KAGRA, Einstein Telescope, and Cosmic Explorer. We assume a source distance of $D = 1$ Mpc. The upper and lower panels are for an observer along the pole and equator, respectively.

observe from equator, rapidly rotating models (R3 and R6) are likely still observable by the third-generation detectors, while it becomes quite hard for slowly rotating models.

GW signals from the anisotropic matter ejection for model R6 appear at a low-frequency range $f \lesssim 10$ Hz for an equatorial observer (red line in the lower panel), which is absent towards the pole. This low-frequency component, whose energy is integrated over 300 ms $\leq t_{\rm pb} \leq 500$ ms according to the top-right panel in Fig. 9, is apparently too weak for the detection. However, if the current anisotropic matter configuration persists longer time, for instance another 1–2 s, the GW emission energy of this low-frequency component can be increased by ~ 5–10 times. Then we can naively expect that those signals can be detected by the third-generation detectors. In the current study, we do not evaluate GWs originated from non-isotropic neutrino radiation. As reported in Müller, Janka & Wongwathanarat (2012a), Vartanyan & Burrows (2020), and Shibagaki et al. (2024), those contributions generally appear at the same low-frequency range ($f \lesssim 10$ Hz). The amplitude can sometimes become by one order of magnitude larger, in particular for rotating models (Shibagaki et al. 2024). This makes their detection even more feasible by the third-generation detectors.

4.2 Neutrino signals

In this section, we first discuss the emergent neutrino profiles and then their observability. Fig. 11 depicts the surface integrated neutrino luminosity L_ν (upper panels) and mean neutrino energy $\langle \varepsilon_\nu \rangle$ for all models except R6o, whose simulation time is too short for the discussion. We show profiles for electron neutrinos ν_e (left), electron

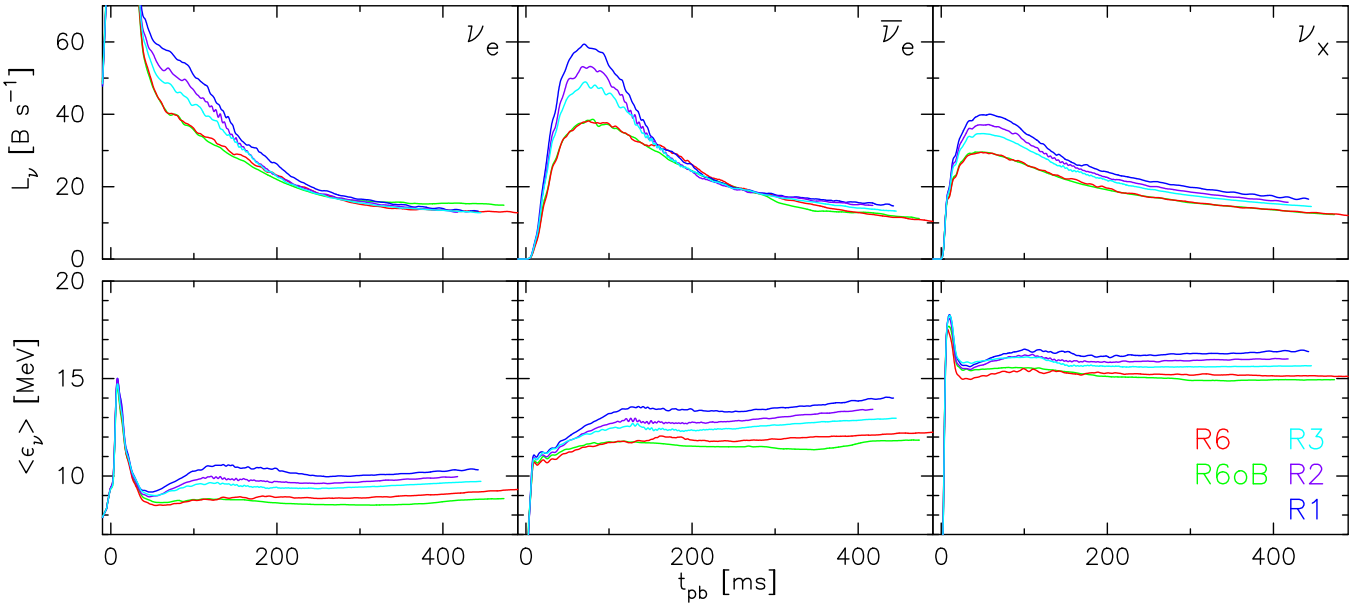

Figure 11. Surface integrated neutrino luminosities (upper panels) and mean neutrino energies for all models except R6o: Electron neutrinos ν_e (left), electron antineutrinos $\bar{\nu}_e$ (middle), and heavy-lepton neutrinos ν_x (right). They are measured on a spherical surface at $r = 400$ km.

antineutrinos $\bar{\nu}_e$ (middle), and heavy-lepton neutrinos ν_x (right), measured on a spherical surface at $r = 400$ km.

In the neutrino luminosities, we find a consistent behaviour with previous electron-capture SN simulations, namely the absence of high accretion luminosities, which is commonly observed also in the collapse of *less* massive stars. For instance, L_{ν_e} for all models present a smooth decline for 50 ms $\lesssim t_{\rm pb} \lesssim$ 200 ms. Such a feature has been reported in previous studies, for instance in electron-capture SNe (Hüdepohl et al. 2010; Radice et al. 2017) or collapse of low mass stars, like 9.6 $M_\odot$ star (Müller & Janka 2014; Kuroda et al. 2022). It stems from the fact that the progenitors of AICs have essentially no envelope and thus no mass accretion. While in the collapse of more massive stars with the mass, e.g. $\gtrsim 10\,M_\odot$, the PNS accretes more mass during this phase, which results in a more prominent, temporal increase of neutrino luminosities at $t_{\rm pb} \sim 100$ ms, in particular for electron neutrinos L_{ν_e} (e.g. Müller, Janka & Heger 2012c; Bollig et al. 2017; Summa et al. 2018; Vartanyan et al. 2019; Kuroda et al. 2022). Neutrino mean energies $\langle\varepsilon_\nu\rangle$ for all flavours present a rather flat evolution after bounce ($t_{\rm pb} \gtrsim 100$ ms). This is a consequence of a nearly saturated PNS mass evolution (see Fig. 2) and associated no significant PNS contraction (besides the contraction associated with long-term neutrino cooling). Without the significant PNS contraction, the neutrino spheres for all flavours do not appreciably propagate inwards and thus the energy spectra of last scattered neutrinos do not significantly evolve, resulting in a nearly constant and relatively lower mean neutrino energies in comparison to normal massive stellar collapse.

As for the rotational effects, we find a clear inverse trend in the ordering of both L_ν and $\langle\varepsilon_\nu\rangle$ with respect to the WD rotation. Neutrino luminosities differ the most during the strong spiral wave phase (50 ms $\lesssim t_{\rm pb} \lesssim$ 200 ms), and afterwards we observe a modest rotational dependence. The mean neutrino energies present ~ 2 MeV difference between the slowest (R1) and fastest (R6) rotating models for all flavours. As a comparison with previous AIC models, our slowest rotating model R1 behaves similarly to an AIC of non-rotating 1.42 $M_\odot$ WD reported in Batziou et al. (2024), albeit during our limited post bounce phase ($t_{\rm pb} \lesssim 500$ ms). Radice et al. (2017)[2] conducted electron-capture SNe using 8.1–8.8 $M_\odot$ progenitor stars and iron core collapse of low-mass ($\sim 10\,M_\odot$) progenitor stars. The present neutrino energy evolutions are similar to those of the former electron-capture SNe (see also Hüdepohl et al. 2010) rather than of the latter iron core collapse of slightly more massive progenitor stars.

Fig. 12 plots the expected neutrino counts in 5 ms bins (solid line) and cumulative counts (dash–dotted) for IceCube (Abbasi et al. 2011; Salathe, Ribordy & Demirörs 2012) (upper panels) and Hyper-Kamiokande (HyperK) (Abe et al. 2011; Hyper-Kamiokande Proto-Collaboration et al. 2018) (lower panels). The neutrino count is evaluated following Lund et al. (2010) for IceCube and Takiwaki & Kotake (2018) for HyperK from surface averaged neutrino luminosities and mean energies of emergent neutrinos, thus simply neglecting the observer angle dependence. We assume a source distance of $D = 10$ kpc. In addition, we consider two cases: a normal mass ordering (NMO: left column) and inverse mass ordering (IMO: right column) (see e.g. Tanabashi et al. 2018, for neutrino mixing parameters used), without taking into account yet-to-be-clarified collective flavor conversions. In the upper panels for IceCube, we also add a random shot noise realization (asterisk) with its standard deviation being $\sim \sqrt{R_{\rm bkgd} \times 5\,[\rm ms]} \sim 86$, where $R_{\rm bkgd} = 1.48 \times 10^3$ ms^{-1} is the assumed background rate of IceCube (e.g. Lund et al. 2010).

From the figure, we notice that the faster rotating models exhibit relatively lower event rates. This trend is simply due to lower neutrino luminosities and mean energies in faster rotating models. The event rate difference between the slowest and fastest rotating models can be as large as about two to three times for both detectors. Our simple estimation for the cumulative number of events infers that if such AICs happen at the Galactic Centre ($D \sim 10$ kpc), we would detect $\sim 10^5$ and $\sim 10^4$ neutrinos for IceCube and HyperK, respectively.

[2]In Radice et al. (2017), they present root-mean-squared neutrino energies, which generally leads to ~ 10 per cent higher energy evaluation than the mean value.

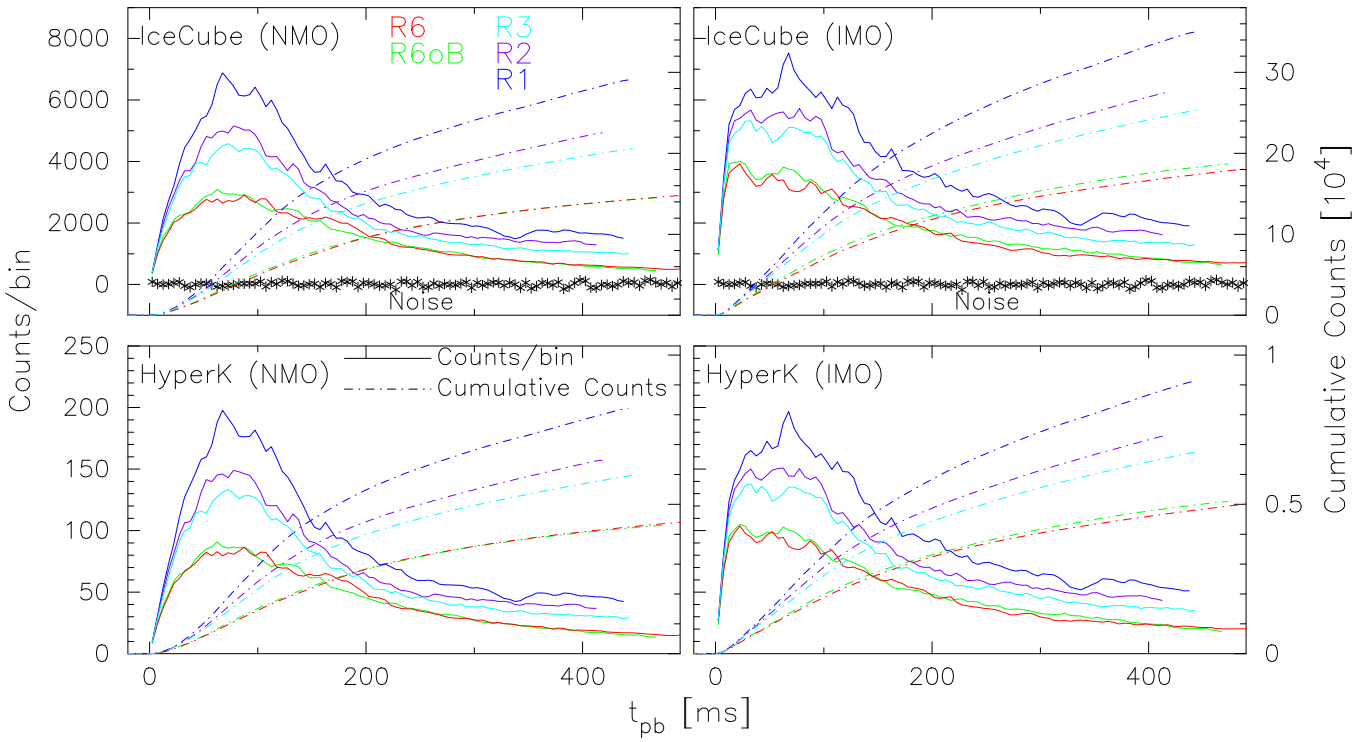

Figure 12. Neutrino counts in 5 ms bin (solid line) and cumulative counts (dash–dotted) for IceCube (upper panels) and for Hyper-Kamiokande (lower panels), assuming a source distance of $D = 10$ kpc. We plot a normal mass ordering (NMO: left column) and inverse mass ordering (IMO: right panels) cases. In the panel for IceCube, we also add a random shot noise realization (asterisk).

These numbers can be more in longer simulation times. A less prominent difference between NMO and IMO cases could be another noteworthy feature of AICs. In typical CCSNe, electron antineutrino luminosity $L_{\bar{\nu}_e}$ is significantly higher than heavy-lepton neutrino luminosity L_x during the accretion phase, which is more pronounced with the increase of the progenitor mass (e.g. Müller & Janka 2014; Vartanyan et al. 2019; Kuroda et al. 2022) and could sometimes result in a factor of 2 difference. On the contrary, $L_{\bar{\nu}_e}$ reported here shows at the largest ~ 50 per cent difference (R1) and moreover the difference soon nearly diminishes, e.g. at $t_{\rm pb} \gtrsim 200$ ms. Consequently, the flavor change has a less impact on the final state as Fig. 12 indicates.

We shortly mention detectability of these AIC events by neutrinos. From Fig. 11, we can naively expect significantly high signal to noise ratio (S/N) for all models for both detectors, if they happen at a source distance of $D = 10$ kpc. Neutrino counts for IceCube ($\gtrsim 1000$ in 5 ms bins) well exceed the background noise ($\lesssim 90$ in 5 ms bins) basically throughout all the simulation time and the same is true for HyperK, which has a background-free signal. From this, we can broadly say that the Galactic events are reasonably observed by neutrinos. However, for more distant events, there will be a point beyond that only HyperK would feasibly detect neutrino signals. For instance, for $D = 20$ kpc, neutrino counts for model R6 at the final simulation time $t_{\rm pb} \sim 500$ ms can be estimated as ~ 130 (IceCube) and ~ 4 (HyperK) in 5 ms bins. Thence, from a very crude estimation, the signal to noise ratio becomes $\sim 130/86 \sim 1.5$ for IceCube, while $\sim 4/\sqrt{4} \sim 2$ for HyperK, where in the latter HyperK case we assume a Poisson error. Additionally, unlike GWs from AICs (see Fig. 10), the expected horizon distance of AICs via neutrino observations is likely much shorter than ~ 1 Mpc. For instance, the cumulative events for HyperK assuming a source distance of $D = 10$ kpc is $\sim 10^4$ at the final simulation time, which becomes ~ 1 if AIC occurs at $D = 1$ Mpc.

4.3 Implications for the electromagnetic counterparts

As described in the introduction, the ejecta formed during the AIC as well as the energy injection from the newborn PNS can be the source of various electromagnetic transients, such as FBOTs. Here, we briefly estimate the property of possible electromagnetic signals in various situations based on the results obtained in this work (see also Drout et al. 2014; Prentice et al. 2018; Rest et al. 2018; Lyutikov & Toonen 2019; Margutti et al. 2019).

Our simulation results suggest that the ejecta mass, explosion energy, and ejecta velocity are of the order of $M_{\rm ej} \sim 0.01$–$0.1\,{\rm M}_\odot$, $E_{\rm exp} \sim 10^{50}$ erg, and $v \sim 0.1\,c$, respectively. The lower limit of the opacity of the ejecta can be given by that of the Thomson scattering $\kappa \sim 0.1\,{\rm cm^2\,g^{-1}}$. The opacity can be increased up to $1\,{\rm cm^2\,g^{-1}}$ for the case that the r-process elements up to the second peak or the first peak are synthesized for 1 per cent ($Y_e \lesssim 0.25$) or 10 per cent ($Y_e \lesssim 0.4$) of the total ejecta mass, respectively (Wanajo et al. 2014; Tanaka et al. 2020). Employing these values, the diffusion time-scale of photons in the ejecta can be estimated as

$$t_{\rm diff} \sim \sqrt{\frac{3\kappa M_{\rm ej}}{4\pi v c}} \approx 3\,{\rm d}\left(\frac{\kappa}{0.2\,{\rm cm^2\,g^{-1}}}\right)^{1/2}\left(\frac{M_{\rm ej}}{0.05\,M_\odot}\right)^{1/2}\left(\frac{v}{0.1\,c}\right)^{-1/2}. \quad (12)$$

Here, the fiducial value for the opacity is set by the case that the opacity is dominated by the Thomson scattering of the matter with $Y_e \approx 0.5$.

For the MIC scenario, the collapse can occur deep inside the inflated envelope of the merger remnant. Schwab (2021) suggests that the envelope extension can vary from $R_* = 10^{10}$ cm to 2×10^{12} cm depending on the total mass of the progenitor system. Under the

assumption that the envelop mass smaller than the ejecta mass, the interaction of the ejecta with the envelope matter results in the cooling emission with the peak luminosity of

$$L_{\rm peak} \sim \frac{E_{\rm exp} t_{\rm e}}{t_{\rm diff}^2} = 3 \times 10^{42} {\rm erg\,s^{-1}} \left(\frac{R_*}{10^{12}\,{\rm cm}}\right) \left(\frac{\kappa}{0.2\,{\rm cm^2\,g^{-1}}}\right)^{-1} \left(\frac{v}{0.1\,c}\right)^2 \quad (13)$$

at the peak time of $t_{\rm diff}$ with the effective temperature of

$$T_{\rm peak} \sim \left(\frac{L_{\rm peak}}{4\pi\sigma_{\rm SB} v^2 t_{\rm diff}^2}\right)^{1/4} \approx 1 \times 10^4\,{\rm K} \left(\frac{R_*}{10^{12}\,{\rm cm}}\right)^{1/4} \times \left(\frac{\kappa}{0.2\,{\rm cm^2\,g^{-1}}}\right)^{-1/2} \left(\frac{M_{\rm ej}}{0.05\,M_\odot}\right)^{-1/4} \left(\frac{v}{0.1\,c}\right)^{1/4}, \quad (14)$$

where $t_{\rm e} = R_*/v$ and $\sigma_{\rm SB}$ is the Stefan–Boltzmann constant. The bolometric luminosity will rapidly decline after the peak with the time-scale of $t_{\rm diff}$, unless there is some energy source that powers the ejecta.

We note that an AIC with an inflated envelope of $R_* \gtrsim 10^{12}$ cm may occur only for a massive remnant (total mass $\approx 1.9\,M_\odot$) (Schwab 2021). For lower-mass WD cases, the progenitor is likely to be significantly contracted by the time of the collapse (Schwab, Quataert & Kasen 2016). In such cases, the interaction between the ejecta and contracted envelope may not produce a bright optical transient, due to the small value of R_* (e.g. Yu, Chen & Wang 2019, see also the reference for the absorption and scattering effects on the emission in the presence of thick wind).

If a significant amount of the *r*-process elements or ^{56}Ni are synthesized in the ejecta, the envelope-ejecta interaction powered emission can be followed by faint long-lasting emission. Although detailed ejecta mass of these heavy elements should be determined by nucleosynthesis calculation, our approximate estimation gives $M_{\rm Ni} = 2.6(2.0) \times 10^{-3}\,{\rm M_\odot}$ for R6(R1), where we presume half of highly heated ejecta beyond 5 GK with $Y_e \geq 0.5$ may become ^{56}Ni (Fujibayashi et al. 2024). Regarding the *r*-process elements, we assume the optimistic case that the *r*-process elements are synthesized for 10 per cent of the total ejecta mass, and thus $M_r = 0.1\,M_{\rm ej}$. With these assumptions, the emission with the peak luminosity of

$$L_{\rm peak} \approx M_{\rm r} \dot{q}_{{\rm r},\beta}(t_{\rm diff}) \approx 1 \times 10^{40}\,{\rm erg\,s^{-1}} \left(\frac{M_{\rm r}}{5 \times 10^{-3}\,{\rm M_\odot}}\right) \left(\frac{t_{\rm diff}}{6\,{\rm d}}\right)^{-1.3} \quad (15)$$

and

$$L_{\rm peak} \approx M_{\rm Ni56} f_\gamma(t_{\rm diff}) \dot{q}_{{\rm Ni56},\gamma}(t_{\rm diff}) \approx 3 \times 10^{40}\,{\rm erg\,s^{-1}} \left(\frac{M_{\rm Ni56}}{3 \times 10^{-3}\,{\rm M_\odot}}\right) \left(\frac{f_\gamma(t_{\rm diff})}{0.1}\right) \times (t_{\rm diff} \ll 9\,{\rm d}) \quad (16)$$

can occur followed by approximately $\propto t^{-1.3}$ and $\propto t^{-3}$ decline rate, respectively (see Fig. 13). Here, $\dot{q}_{{\rm r},\beta} \approx 10^{10}\,{\rm erg\,g^{-1}\,s^{-1}} \left(\frac{t}{\rm d}\right)^{-1.3}$ and $\dot{q}_{{\rm Ni56},\gamma} \approx 3 \times 10^{10}\,{\rm erg\,g^{-1}\,s^{-1}}$ ($t \ll 9$ d) denote the specific radioactive decay heating rates of the *r*-process elements (β particles) (Korobkin et al. 2012) and ^{56}Ni, respectively. $t_{\rm diff}$ for the *r*-process powered emission model is modified so as to take the increase in the opacity into account ($\kappa = 1\,{\rm cm^2 g^{-1}}$). Note that, while the energy deposition with β particles of the *r*-process elements is well thermalized up to 70 d (Barnes et al. 2016), thermalization of deposited γ-rays is less efficient after $t_{\rm ineff} \sim 1$ day for the γ-ray effective opacity

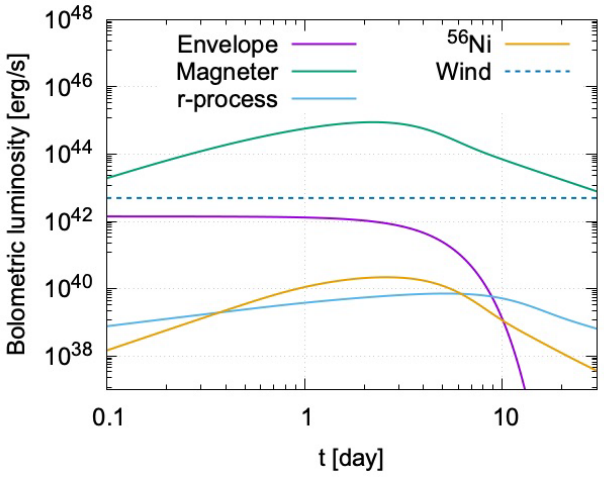

Figure 13. Light curves associated with an AIC for various scenarios obtained by numerically solving one-zone models.

of $0.027\,{\rm cm^2\,g^{-1}}$ (Maeda 2006) for the typical ejecta parameters. Hence, the thermalization efficiency of $f_\gamma = 1 - e^{-t_{\rm ineff}^2/t^2}$ (Barnes et al. 2016) is taken into account for the ^{56}Ni powered emission. These results here with equation (13) suggest that if the radius of the extended envelope is smaller than $\sim 10^{10}$ cm, the peak luminosity will be dominated by radioactive decay powered emission with this hypothetical amount of *r*-process elements or ^{56}Ni. The photospheric temperature at the peak can be estimated from equations (15) and (16) to be $T_{\rm peak} \approx 2$–3×10^3 K, which suggests that the emission is bright in the near-infrared wavelengths: The emission from radioactively powered AIC ejecta may appear similar to that of a faint, red kilonova. Distinguishing this emission from an NS merger kilonova will likely require the detailed spectral modelling.

Direct measurements of the radioactive-decay gamma-rays escaping from ejecta may provide the proof for the presence and identification of the nucleosynthesis of radioactive elements (Patel et al. 2025). However, for the plausible amount of synthesized *r*-process elements and ^{56}Ni, the gamma-ray luminosity will be too faint to be detected by the current missions (Hotokezaka et al. 2016) unless the event occurs at a very close distance ($\lesssim 1$ Mpc). Nevertheless, the observation by new detectors with the sensitivity improved by an order of magnitude will be a powerful tool for diagnosing nucleosynthesis in AIC ejecta.

The magnetar activity of a newborn NS can also power the ejecta and may be the source of rapidly evolving luminous transients (Yu et al. 2015). The magnetar could be well formed in the aftermath of AIC/MICs, if the collapsing initial WDs are sufficiently magnetized and rapidly rotating. It is indeed still a matter of debate how such strongly magnetized WDs ($\gtrsim 10^{10}$ G) are feasibly formed in the stellar evolution scenario (see Zhu et al. 2015, for a potential magnetic field amplification process via merger of WDs). Unfortunately, because their focus was on the formation of sub-Chandrasekhar mass WDs, we cannot directly apply their results to AIC/MICs and associated magnetar formation of our current interest. However, presuming strong magnetic fields ($\gtrsim 10^{10}$ G) inside super-Chandrasekhar mass WDs, the magnetar might be reasonably formed. This is because those initial fields are first amplified via compression during the collapse by 2–3 orders of magnitude and then additionally by rotational winding and possibly some other non-linear processes, e.g. MRI (Balbus & Hawley 1991). For instance by rotational winding alone, the compressed magnetic fields are further amplified

by 1–2 orders of magnitude during a time-scale of ∼10–100 ms, if the nascent NS's rotation period is 1 kHz. As a result, the initial magnetic fields could be well amplified in total by 4–5 orders of magnitude, i.e. the magnetar class ∼ 10^{14-15} G, within a dynamically relevant time-scale (e.g. within ∼ 100 ms after bounce). Our rotating magnetized WD model R6oB, which assumes a rather stronger initial poloidal (dipole-like configuration) magnetic field strength of 10^{11} G, achieves $B_{\rm p} \sim 10^{14-15}$ G and toroidal component $B_\phi \sim 10^{16}$ G inside PNS with a spin period of $\Omega \geq 1000\,{\rm rad\,s^{-1}}$.

In the following discussion, we, therefore, employ the NS dipole magnetic field strength of $B_{\rm p} = 10^{15}$ G and NS rotation angular frequency of $\Omega = 1000\,{\rm rad\,s^{-1}}$ as fiducial values. These values are indeed indicated for explaining the peak luminosity of $L_{\rm peak} \sim 10^{44}\,{\rm erg\,s^{-1}}$, which is thus associated with particularly luminous events within the observed range ($L_{\rm peak} \sim 10^{42-44}\,{\rm erg\,s^{-1}}$, Drout et al. 2014), and the energy injection from the magnetar to the ejecta can be written in the form of $L_{\rm mag} = L_{\rm mag,0}/(1 + t/\tau_{\rm mag})^2$, where the initial spin down luminosity, $L_{\rm mag,0}$, and time-scale, $\tau_{\rm mag}$, are given by

$$L_{\rm mag,0} \sim \frac{B_{\rm p}^2 R_{\rm NS}^6 \Omega^4}{6c^3} \approx 2\times10^{46}\,{\rm erg\,s^{-1}} \left(\frac{B_{\rm p}}{10^{15}\,{\rm G}}\right)^2 \times \left(\frac{R_{\rm NS}}{12\,{\rm km}}\right)^6 \left(\frac{\Omega}{1000\,{\rm rad\,s^{-1}}}\right)^4 \quad (17)$$

and

$$\tau_{\rm mag} \approx 0.6\,{\rm d} \left(\frac{B_{\rm p}}{10^{15}\,{\rm G}}\right)^{-2} \left(\frac{M_{\rm NS}}{1.6\,{\rm M_\odot}}\right) \times \left(\frac{R_{\rm NS}}{12\,{\rm km}}\right)^{-6} \left(\frac{I_{\rm NS}}{2\times10^{45}{\rm g\,cm^2}}\right) \left(\frac{\Omega}{1000\,{\rm rad\,s^{-1}}}\right)^{-2}, \quad (18)$$

respectively. Then, the peak luminosity of magnetar powered emission at $t = t_{\rm diff}$ can be estimated as (Kasen & Bildsten 2010)

$$L_{\rm peak} \approx 2\times10^{45}\,{\rm erg\,s^{-1}} \left(\frac{B_{\rm p}}{10^{15}\,{\rm G}}\right)^{-2} \left(\frac{M_{\rm NS}}{1.6\,{\rm M_\odot}}\right) \times \left(\frac{R_{\rm NS}}{12\,{\rm km}}\right)^{-6} \left(\frac{I_{\rm NS}}{2\times10^{45}{\rm g\,cm^2}}\right)^2 \left(\frac{t_{\rm diff}}{2\,{\rm d}}\right)^{-2} \times(\tau_{\rm mag} < t_{\rm diff}). \quad (19)$$

Here, $M_{\rm NS}$, $R_{\rm NS}$, and $I_{\rm NS}$ denote the NS mass, radius, and moment of inertia and we employ fiducial values of $M_{\rm NS} = 1.6\,{\rm M_\odot}$, $\rm R_{NS} = 12\,km$, and $I_{\rm NS} = 2\times10^{45}\,{\rm g\,cm^2}$ in the above expression. We note that, from our numerical models, $M_{\rm NS}$(∼ 1.6–1.7 $\rm M_\odot$) is nearly saturated even during our simulation time of ≤ 500 ms (Fig. 2) and is consistent with the value assumed above. However, regarding $R_{\rm NS}$ and $I_{\rm NS}$, our simulation results give the values relevant only for the PNS phase, which are $R_{\rm NS} \sim 20$ km (on axis) and ≳ 100 km (equator) and $I_{\rm NS} \sim 10^{46}\,{\rm g\,cm^2}$ at the final simulation time and significantly differ from values assumed, though these PNS properties will change along with the subsequent deleptonization of NS ($t_{\rm pb} \gg 10$ s). We also note that the photon diffusion time-scale is modified by updating the ejecta velocity by $v \to \sqrt{2(E_{\rm exp} + L_{\rm mag,0}\tau_{\rm mag})/M_{\rm ej}} \sim \sqrt{I\Omega^2/M_{\rm ej}}$ considering the ejecta acceleration due to the energy injection from the magnetar (see Kasen & Bildsten 2010). We also note that equation (19) is only valid for the case that the diffusion time-scale is longer than the spin-down time-scale.

Finally, we consider the emission of the shock breakout in the progenitor stellar wind (Balberg & Loeb 2011) as well as the emission powered by the wind-ejecta interaction (Moriya et al. 2013). Assuming that the AIC occurs in a wind density profile given by $\rho_{\rm wind} = A/r^2$ with A being an assumed coefficient determined by the mass-loss rate and stellar wind velocity and r referring the distance from the event, the peak time and shock luminosity at the peak time of the shock breakout emission can be estimated as (Balberg & Loeb 2011; Margutti et al. 2019)

$$t_{\rm peak} \sim \frac{\kappa A}{c} \approx 4\times10^{-3}\,{\rm day} \left(\frac{\kappa}{0.2\,{\rm cm^2\,g^{-1}}}\right)\left(\frac{A}{10^2\,A_*}\right) \quad (20)$$

and

$$L_{\rm sh} \sim \frac{9\pi}{8} r^2 \rho_{\rm wind} v^3 = 5\times10^{42}\,{\rm erg\,s^{-1}} \left(\frac{A}{10^2 A_*}\right)\left(\frac{v}{0.1\,c}\right)^3, \quad (21)$$

respectively, with $A_* = 5\times10^{11}\,{\rm g\,cm^{-1}}$ which corresponds to the case of the wind mass-loss rate of $\dot{M} = 10^{-5}\,{\rm M_\odot\,yr^{-1}}$ and wind velocity of $v_{\rm wind} = 10^3\,{\rm km\,s^{-1}}$. The naive estimation of the effective temperature at the peak time is 3×10^5 K. However, since the shock velocity is larger than $0.07\,c$, the actual emission will be bright in X-ray (≳ 1 keV) due to insufficient thermalization (Katz, Budnik & Waxman 2010; Nakar & Sari 2010). For the wind profile $\propto r^{-2}$, the shock luminosity will remain approximately constant and power the emission until the stopping time of the ejecta, which is estimated by $\approx 6\times10^2\,{\rm d}(M_{\rm ej}/0.05\,{\rm M_\odot})(v/0.1\,c)^{-1}(A/10^2\,A_*)$ from $M_{\rm ej} \approx \int_0^{vt} 4\pi r^2 \rho_{\rm wind} {\rm d}r$. However, the efficiency of converting the matter internal energy into photon energy may become inefficient in the later epoch (Moriya et al. 2013). Hence, the value of $L_{\rm sh}$ should be taken as the upper limit of the photon luminosity after the shock breakout time.

Fig. 13 shows the light curves obtained by numerically solving one-zone models of the scenarios discussed above. In the one zone models, the evolution of the internal energy, $E_{\rm int}$, is carried out under the assumption of homogeneous density, radiation dominated pressure, and homologously expanding velocity profile of ejecta. The evolution equation for $E_{\rm int}$ is given by (e.g. Kasen & Bildsten 2010)

$$\frac{{\rm d}E_{\rm int}}{{\rm d}t} = -\frac{E_{\rm int}}{t} - L_{\rm rad} + H_{\rm heat}, \quad (22)$$

where $L_{\rm rad} \sim E_{\rm int} t/t_{\rm diff}^2$ and $H_{\rm heat}$ denote the bolometric luminosity and total energy injection rate, respectively. The parameters as well as the total energy injection rate used in the model of each scenario are the same as those employed in the discussion above. The values of the peak luminosity estimated above are indeed approximately reproduced by the one-zone models.

With the ejecta property obtained by our work, the energy injection from the newborn magnetar can explain the brighter side of observed FBOTs, whose bolometric luminosities peak at $\gtrsim 10^{44}\,{\rm erg\,s^{-1}}$, as being pointed out by previous studies (Prentice et al. 2018; Rest et al. 2018; Lyutikov & Toonen 2019; Margutti et al. 2019). However, the brightness and time-scale of the emission are highly dependent on the property of the newborn magnetar, and hence, the investigation of the magnetar property based on plausible AIC/MIC progenitor models and considering relevant magnetic field amplification mechanisms will be crucial for the light curve prediction.

Even in the absence of a magnetar formation, there could be various electromagnetic counterparts (see also, e.g. Margutti et al. 2019). The cooling emission due to the ejecta-envelope interaction can explain the faint FBOT peak luminosities of $\sim 10^{42}\,{\rm erg\,s^{-1}}$ (Drout et al. 2014), if the envelope radius R_* is larger than 10^{12} cm. The emission will decay rapidly in the time-scale of a few days unless a significant energy injection is present. Hence, in the case of observing the FBOT-like transient, the presence of a power source can be distinguished by the observation on whether the

luminosity rapidly drops within a few times the peak time-scale or not.

The long-lasting emission followed by such a rapid decline after a few diffusion time-scales (~ 10 day) may indicate the production of the *r*-process elements or ^{56}Ni in the AIC ejecta. Due to the small ejecta mass and resulting inefficient γ-ray thermalization, the emission powered by ^{56}Ni can decline more rapidly than that powered by the *r*-process heating, while the actual decline rate of the *r*-process powered emission can also strongly depend on the nucleosynthetic abundances (Wanajo et al. 2014). For observing such signals, the deep follow-up observation in the infrared wavelengths, such as by *JWST*, will be needed also with the nebular spectral modelling (Hotokezaka et al. 2023; Pognan et al. 2023), since the ejecta are expected to be optically thin after 10 day. For example, assuming that the nebular spectra observed in GRB230307A (Levan et al. 2024) was powered by radioactive decay of *r*-process elements with ejecta mass $\sim 0.05\,M_\odot$ in the distance of 300 Mpc, the nebular phase emission powered by radioactive decay may be observed for nearby AIC events with the distance < 100 Mpc if the sufficiently large amount of *r*-process elements ($> 0.005\,M_\odot$) is synthesized.

The AIC ejecta-wind interaction can result in the shock-breakout emission comparably bright to some of FBOTs, as far as the mass-loss rate is larger than $10^{-3}\,M_\odot\,\mathrm{yr}^{-1}$. However, as seen above as well as being pointed out in Margutti et al. (2019), significantly higher wind density (with 0.1–1 $M_\odot\,\mathrm{yr}^{-1}$) will be required to explain bright FBOTs with $> 10^{44}\,\mathrm{erg\,s}^{-1}$. Since the emission will be bright in X-rays, wide-field time-domain X-ray telescopes, such as Einstein Probe (Yuan et al. 2022; Yuan et al. 2025), will be useful to observe the shock-breakout emission. For example, the shock breakout emission peaks with the time-scale of 1000 s with the brightness of $\sim 10^{43}\,\mathrm{erg\,s}^{-1}$ can be detected for the events with the distance $\lesssim 50$ Mpc by the WXT (Yuan et al. 2025; see also references therein for the expected detection rate of FBOTs by Einstein Probe), while the detectability should be discussed employing more detailed modelling of the emission (Nakar & Sari 2010). The spectral features of the emission induced by the wind-ejecta interaction can indicate the progenitor of the system. For example, no H/He line feature is expected in the spectra if the progenitor is formed through a merger with its companion WD (Saio & Nomoto 1985; Shen et al. 2012; Schwab 2021), whereas such features can be present if the companion is a non-degenerate star with an H/He layer (Nomoto et al. 1979; Nomoto & Kondo 1991). Note, however, that if the wind shell has already detached far from the progenitor surface at the onset of the AIC, both shock-breakout and shock-powered emission in the early phase may be absent (Yu et al. 2019). Nevertheless, the presence of the dense stellar wind can still be confirmed by observing radio synchrotron emission, which may peak around the ejecta deceleration time-scale (100–1000 d for the $A = 10^2\,A_*$ wind profile; Margutti et al. 2019, see also Yu et al. 2019).

The increase in the ejecta opacity due to the presence of the *r*-process elements in general leads to the emission with the fainter luminosity, redder spectra, and longer time-scale (see e.g. equations 13, 14, and 12). In fact, the peak luminosity can be fainter for an order of magnitude in the presence of large amount of the *r*-process elements, and diffusion time-scale and effective temperature at the peak can also be longer and lower by a factor of a few, respectively. While the estimation of the ejecta opacity can be a good indicator for the significant production of the *r*-process elements, its dependence also degenerates with other model parameters, such as the envelope radius, magnetar properties, and wind profiles. Hence, in order to judge the presence of the *r*-process elements, more detailed modelling of the observations, such as light curve/spectral evolutions, also with the accurate predictions is necessary.

5 SUMMARY

We presented the results of 3D numerical relativity simulations with multi-energy neutrino transport for core collapse of rotating magnetized WDs, as a modelling for an end stage of single or double degenerate WD evolutions. The main focuses of this study are on the explosion dynamics and their associated multimessenger signals: GWs, neutrinos, and electromagnetic counterparts. AIC of WDs has been recently attracting more attentions because of their unique properties (relatively low explosion energy and small amount of mass ejection), which might be feasible to explain some of the rapidly evolving optical transients. Our results indeed support such scenarios, albeit depending on yet-to-be-cleared several parameters assumed.

Regarding the explosion dynamics, we witnessed prompt type explosions in all models. The shock front does not noticeably stall and it reaches 10^9 cm at $t_{\rm pb} \sim 300$ ms. All models including the slowest rotating one R1 show a bipolar explosion, with R6 presenting the most visible jet-like configuration. At the end of our simulation times ($t_{\rm pb} \sim 400$–500 ms), the diagnostic explosion energy and ejecta mass reach 0.1–0.4 B and 0.02–0.1 $M_\odot$, respectively. These values are in good agreement with latest reports (Longo Micchi et al. 2023; Batziou et al. 2024; Cheong et al. 2025) and indeed fall in the range of low explosion energy and small ejecta mass in comparison to typical massive stellar collapse cases. As for the rotational dependence on the shock dynamics, rapidly rotating models initially exhibit larger shock radii due mainly to centrifugal expansion. However at a later phase, moderately rotating models show more extended shock radii, which are facilitated by stronger neutrino heating emitted from more compact and hotter PNS because of the less centrifugal support. As another remarkable feature of rotation, our rapidly rotating model R6 presents the emergence of strong spiral waves dominated by a low (one-armed) mode, which is by definition completely suppressed in the counterpart octant symmetry model R6o. These spiral waves play a role to increase both the explosion energy and ejecta mass approximately by a factor of 2, from which we can say that full 3D models, i.e. without assuming axisymmetry, are essential.

We also discussed ejecta properties. As a major trend, the faster rotating model ejects lower Y_e components, which is consistent with Batziou et al. (2024). There are two rotational effects which produce such a trend. As a leading effect, the rotation simply flattens the central core having low-Y_e matters towards equator. Thence the edge of such a core, particularly along the equator, becomes gravitationally loosely bound and is consequently more easily ejected. The appearance of strong spiral waves may also be another factor, as such kind of rotational instability redistributes the angular momentum and the low-Y_e matters in the vicinity of central core tend to be more easily expelled. Typical ejecta velocities and Y_e extend from 0.05 to 0.1 c and ~ 0.3 to well above 0.5, respectively.

The strong spiral waves are indeed the origin of loud GW signals. The most rapidly rotating model R6 emits GWs, whose amplitudes reach $D|h| \sim 500$ cm for an observer along the rotational axis, during the spiral-wave developing phase. These signals are not burst type GWs, as represented by the so-called Type I signal from the rotational core bounce, but last for a relatively long time, broadly 100 ms in all models. Such long-lasting quasi-periodic strong signals may expand the horizon distance of such events for GWs up to ~ 1 Mpc for the current generation GW detectors or even up to ~ 10 Mpc for third-generation ground-based detectors, which

can be assessed by more sophisticated GW detection analyses. We also found a new finding that the dominant mode of spectral evolution is consisted of two components: initial spiral wave-origin modes and subsequent ramp-up feature stemming from g/f-mode oscillations of 'rotationally flattened' PNS core. According to our mode analysis, the initial peak frequency associated with the spiral waves are nicely explained by the typical rotational frequency of a region (more precisely a shell of rotating spheroid), whose density is around $\sim 10^{13}\,\mathrm{g\,cm^{-3}}$ regardless of the initial rotation. After the fade-out of the strong spiral waves, the spectral peak is smoothly taken over by those of g/f-mode oscillations. We demonstrated that the PNS radius and emergent electron antineutrino energy $\varepsilon_{\bar{\nu}_e}$, which are often used to describe the ramp-up feature of g/f-mode oscillations (Marek, Janka & Müller 2009; Müller et al. 2013), can be measured along the pole to reproduce the spectral evolution.

We also discussed how we would be able to observe such AIC events via neutrinos. Because of the nature of AICs with essentially no stellar envelope, the mass accretion onto the nascent NS is largely suppressed compared to typical massive stellar collapse. As a result, the accretion luminosity phase soon ceases and neutrino luminosities for all species become relatively fainter. Additionally the evolution of mean energy of emergent neutrinos does not present any noticeable increasing trend. All these features are quite similar to those from iron core collapse at low mass end or electron-capture SNe (Hüdepohl et al. 2010; Müller & Janka 2014; Radice et al. 2017; Kuroda et al. 2022). As another feature, we did not observe any significant differences in neutrino detection rates between normal and inverse mass ordering. This stems again from the low-mass accretion rate in AICs, which results in the aforementioned less distinction in neutrino profiles between different neutrino flavours. Our simple estimation infers that if such AICs happen at the Galactic Centre, we would detect $\sim 10^5$ and $\sim 10^4$ neutrinos for IceCube and HyperK, respectively. For IceCube, the neutrino counts are well above its background signal, if they happen at the Galactic Centre. However, unlike the horizon distance of such events for GWs ($\sim$ 10(1) Mpc for the third(current) generation detectors), relatively faint neutrino luminosity makes its horizon distance much shorter than 1 Mpc.

Based on the simulation results, we broadly estimated the properties of possible electromagnetic counterparts in various scenarios which can be associated to AICs. With tuned properties of the newborn magnetar, the energy injection from the magnetar can explain the FBOTs with the ejecta property obtained in our work, as being pointed out by previous studies (Drout et al. 2014; Prentice et al. 2018; Rest et al. 2018; Lyutikov & Toonen 2019; Margutti et al. 2019). Even in the absence of the significant magnetar energy injection to the ejecta, the cooling emission due to the ejecta-envelope interaction can be as bright as some of faint FBOTs (Drout et al. 2014) with the inflated envelope of $\gtrsim 10^{12}$ cm. The cooling envelope emission can be followed by the nebular emission powered by r-process elements or ^{56}Ni productions. The observation of these signals will provide important insights into the diversity in AICs as well as their potential roles in the chemical evolution in the universe. Since the light curves are highly dependent on the assumption on the magnetar, the investigation of its property consistently following its formation process taking the magnetic field effects into account is crucial. In addition, more sophisticated modelling based on the detailed structure and neucleosynthetic abundances of the ejecta as well as taking microphysical process (e.g. Nakar & Sari 2010; Hotokezaka et al. 2023; Pognan et al. 2023) and multidimensional radiative transfer effects (e.g. Margutti et al. 2019) into account is needed to provide accurate light curve/spectral predictions, which are left as topics for future investigation.

Before closing, we shortly touch on observable differences in multimessenger signals between AIC and BNS, both of which could be the potential formation channel to a rapidly rotating NS. Regarding their GWs, BNS emits typically two to three orders of magnitude larger amplitudes than those from collapse of WDs, with significantly different waveforms (e.g. Shibata, Taniguchi & Uryū 2005). We also expect noticeable differences in neutrino signals at bounce in AICs or at merger in BNSs. On one hand the former AIC exhibits the electron type neutrino burst at core-bounce via deleptonization, the BNS merger, on the other hand, emits electron type antineutrino burst (Cusinato et al. 2022) due to leptonization. Finally as for the EM counterpart, the AIC may exhibit some features of its companion star, for instance H/He line feature is expected in the spectra if the companion is a non-degenerate star with an H/He layer (Nomoto et al. 1979; Nomoto & Kondo 1991), which is surely absent in the BNS merger. As we discussed, the emission from radioactively powered AIC ejecta may appear similar to that of a faint, red kilonova, although we certainly need more detailed nucleosynthesis calculation as well as spectral modelling. Like these, we can expect that there are many distinct features in the multimessenger signals between AIC and BNS, which would enable us to easily distinguish these two events.

ACKNOWLEDGEMENTS

TK thanks the members of the CRA for stimulated discussion and useful advice. TK is also grateful to Tobias Fischer for the extended EOS tables and also to Shota Shibagaki for providing a module to reproduce the background shot noise for IceCube. We also acknowledge Brian Metzger for his valuable comments on the observed properties of AT 2018cow. Numerical computations were carried out on Sakura and Raven at Max Planck Computing and Data Facility. This work was in part supported by Grant-in-Aid for Scientific Research (No. 23H04900) of Japanese MEXT/JSPS.

DATA AVAILABILITY

The data underlying this article will be shared on reasonable request to the corresponding author. GW strains and neutrino profiles used in Figs 9 and 11, respectively, are available in an online repository https://github.com/kurodatk/GWs_Neutrinos_AIC.

REFERENCES

Abbasi R. et al., 2011, A&A, 535, A109
Abbott B. P. et al., 2017, Class. Quantum Gravity, 34, 044001
Abbott B. P. et al., 2018, Living Rev. Relat., 21, 3
Abdikamalov E. B., Ott C. D., Rezzolla L., Dessart L., Dimmelmeier H., Marek A., Janka H. T., 2010, Phys. Rev. D, 81, 044012
Abe K. et al., 2011, preprint (arXiv:1109.3262)
Balberg S., Loeb A., 2011, MNRAS, 414, 1715
Balbus S. A., Hawley J. F., 1991, ApJ, 376, 214
Barnes J., Kasen D., Wu M.-R., Martínez-Pinedo G., 2016, Astrophys. J., 829, 110
Baron E., Cooperstein J., Kahana S., Nomoto K., 1987, ApJ, 320, 304
Batziou E., Glas R., Janka H. T., Ehring J., Abdikamalov E., Just O., 2025, ApJ, 984, 197
Baumgarte T. W., Shapiro S. L., 1999, Phys. Rev. D, 59, 024007
Bollig R., Janka H. T., Lohs A., Martínez-Pinedo G., Horowitz C. J., Melson T., 2017, Phys. Rev. Lett., 119, 242702

Bugli M., Guilet J., Obergaulinger M., Cerdá-Durán P., Aloy M. A., 2020, MNRAS, 492, 58
Centrella J. M., New K. C. B., Lowe L. L., Brown J. D., 2001, ApJ, 550, L193
Cheong P. C.-K., Pitik T., Longo Micchi L. F., Radice D., 2025, ApJ, 978, L38
Cusinato M., Guercilena F. M., Perego A., Logoteta D., Radice D., Bernuzzi S., Ansoldi S., 2022, Eur. Phys. J. A, 58, 99
Dan M., Rosswog S., Brüggen M., Podsiadlowski P., 2014, MNRAS, 438, 14
Dessart L., Burrows A., Ott C. D., Livne E., Yoon S. C., Langer N., 2006, ApJ, 644, 1063
Di Stefano R., Voss R., Claeys J. S. W., 2011, ApJ, 738, L1
Dimmelmeier H., Font J. A., Müller E., 2002, A&A, 393, 523
Dimmelmeier H., Ott C. D., Marek A., Janka H.-T., 2008, Phys. Rev. D, 78, 064056
Drout M. R. et al., 2014, ApJ, 794, 23
Fryer C., Benz W., Herant M., Colgate S. A., 1999, ApJ, 516, 892
Fujibayashi S., Sekiguchi Y., Shibata M., Wanajo S., 2023, ApJ, 956, 100
Fujibayashi S., Lam A. T.-L., Shibata M., Sekiguchi Y., 2024, Phys. Rev. D, 109, 023031
García-Berro E. et al., 2012, ApJ, 749, 25
Hachisu I., Eriguchi Y., Nomoto K., 1986, ApJ, 308, 161
Hild S. et al., 2011, Class. Quantum Gravity, 28, 094013
Hilditch D., Bernuzzi S., Thierfelder M., Cao Z., Tichy W., Brügmann B., 2013, Phys. Rev. D, 88, 084057
Hotokezaka K., Wanajo S., Tanaka M., Bamba A., Terada Y., Piran T., 2016, MNRAS, 459, 35
Hotokezaka K., Tanaka M., Kato D., Gaigalas G., 2023, MNRAS, 526, L155
Hüdepohl L., Müller B., Janka H. T., Marek A., Raffelt G. G., 2010, Phys. Rev. Lett., 104, 251101
Hyper-Kamiokande Proto-Collaboration, 2018, Prog. Theor. Exp. Phys., 2018, 063C01
Inserra C., 2019, Nat. Astron., 3, 697
Just O., Bauswein A., Ardevol Pulpillo R., Goriely S., Janka H. T., 2015, MNRAS, 448, 541
Kasen D., Bildsten L., 2010, ApJ, 717, 245
Katz B., Budnik R., Waxman E., 2010, ApJ, 716, 781
Korobkin O., Rosswog S., Arcones A., Winteler C., 2012, MNRAS, 426, 1940
Kotake K., Takiwaki T., Fischer T., Nakamura K., Martínez-Pinedo G., 2018, ApJ, 853, 170
Kuroda T., 2021, ApJ, 906, 128
Kuroda T., Shibata M., 2024, MNRAS, 533, L107
Kuroda T., Takiwaki T., Kotake K., 2014, Phys. Rev. D, 89, 044011
Kuroda T., Kotake K., Takiwaki T., 2016, ApJ, 829, L14
Kuroda T., Arcones A., Takiwaki T., Kotake K., 2020, ApJ, 896, 102
Kuroda T., Fischer T., Takiwaki T., Kotake K., 2022, ApJ, 924, 38
Levan A. J., et al., 2024, Nature, 626, 737
Longo Micchi L. F., Radice D., Chirenti C., 2023, MNRAS, 525, 6359
Lund T., Marek A., Lunardini C., Janka H.-T., Raffelt G., 2010, Phys. Rev. D, 82, 063007
Lyutikov M., Toonen S., 2019, MNRAS, 487, 5618
Maeda K., 2006, ApJ, 644, 385
Maggiore M., 2007, Gravitational Waves: Volume 1: Theory and Experiments. Oxford Univ. Press, Oxford
Marek A., Janka H.-T., Müller E., 2009, A&A, 496, 475
Margutti R. et al., 2019, ApJ, 872, 18
Marsh T. R., Nelemans G., Steeghs D., 2004, MNRAS, 350, 113
Mezzacappa A. et al., 2020, Phys. Rev. D, 102, 023027
Mor R., Livne E., Piran T., 2023, MNRAS, 518, 623
Mori M., Sawada R., Suwa Y., Tanikawa A., Kashiyama K., Murase K., 2025, PASJ, 77, 127
Moriya T. J., Blinnikov S. I., Tominaga N., Yoshida N., Tanaka M., Maeda K., Nomoto K., 2013, MNRAS, 428, 1020
Morozova V., Piro A. L., Valenti S., 2018, ApJ, 858, 15
Müller B., Janka H.-T., 2014, ApJ, 788, 82
Müller E., Janka H.-T., Wongwathanarat A., 2012a, A&A, 537, A63
Müller B., Janka H.-T., Marek A., 2012b, ApJ, 756, 84
Müller B., Janka H.-T., Heger A., 2012c, ApJ, 761, 72
Müller B., Janka H.-T., Marek A., 2013, ApJ, 766, 43
Murphy J. W., Ott C. D., Burrows A., 2009, ApJ, 707, 1173
Nakar E., Sari R., 2010, ApJ, 725, 904
Nomoto K., Kondo Y., 1991, ApJ, 367, L19
Nomoto K., Nariai K., Sugimoto D., 1979, PASJ, 31, 287
Obergaulinger M., Aloy M. Á., 2020, MNRAS, 492, 4613
Obergaulinger M., Aloy M. Á., 2021, MNRAS, 503, 4942
Obergaulinger M., Aloy M. A., Dimmelmeier H., Müller E., 2006, Astron. Astrophys., 457, 209
Ott C. D., Ou S., Tohline J. E., Burrows A., 2005, ApJ, 625, L119
Ott C. D., Dimmelmeier H., Marek A., Janka H. T., Hawke I., Zink B., Schnetter E., 2007, Phys. Rev. Lett., 98, 261101
Pasham D. R. et al., 2021, Nat. Astron., 6, 249
Patel A., Metzger B. D., Cehula J., Burns E., Goldberg J. A., Thompson T. A., 2025, ApJ, 984, L29
Pognan Q., Grumer J., Jerkstrand A., Wanajo S., 2023, MNRAS, 526, 5220
Prentice S. J. et al., 2018, ApJ, 865, L3
Pursiainen M. et al., 2018, MNRAS, 481, 894
Radice D., Burrows A., Vartanyan D., Skinner M. A., Dolence J. C., 2017, ApJ, 850, 43
Reboul-Salze A., Barrère P., Kiuchi K., Guilet J., Raynaud R., Fujibayashi S., Shibata M., 2025, A&A, 699, A4
Rest A. et al., 2018, Nat. Astron., 2, 307
Saijo M., Yoshida S., 2006, MNRAS, 368, 1429
Saio H., Nomoto K., 1985, A&A, 150, L21
Saio H., Nomoto K., 2004, ApJ, 615, 444
Salathe M., Ribordy M., Demirörs L., 2012, Astropart. Phys., 35, 485
Scheidegger S., Käppeli R., Whitehouse S. C., Fischer T., Liebendörfer M., 2010, A&A, 514, A51
Schmidt G. D. et al., 2003, ApJ, 595, 1101
Schwab J., 2021, ApJ, 906, 53
Schwab J., Quataert E., Kasen D., 2016, MNRAS, 463, 3461
Segretain L., Chabrier G., Mochkovitch R., 1997, ApJ, 481, 355
Shen K. J., Bildsten L., Kasen D., Quataert E., 2012, ApJ, 748, 35
Shibagaki S., Kuroda T., Kotake K., Takiwaki T., 2021, MNRAS, 502, 3066
Shibagaki S., Kuroda T., Kotake K., Takiwaki T., Fischer T., 2024, MNRAS, 531, 3732
Shibata M., Nakamura T., 1995, Phys. Rev. D, 52, 5428
Shibata M., Sekiguchi Y.-I., 2003, Phys. Rev. D, 68, 104020
Shibata M., Sekiguchi Y.-I., 2004, Phys. Rev. D, 69, 084024
Shibata M., Sekiguchi Y.-I., 2005, Phys. Rev. D, 71, 024014
Shibata M., Karino S., Eriguchi Y., 2002, MNRAS, 334, L27
Shibata M., Karino S., Eriguchi Y., 2003, MNRAS, 343, 619
Shibata M., Taniguchi K., Uryū K., 2005, Phys. Rev. D, 71, 084021
Shibata M., Liu Y. T., Shapiro S. L., Stephens B. C., 2006, Phys. Rev. D, 74, 104026
Shibata M., Kiuchi K., Sekiguchi Y., Suwa Y., 2011, Progr. Theor. Phys., 125, 1255
Smartt S. J. et al., 2018, Astron. Telegram, 11727, 1
Sotani H., Takiwaki T., 2020, MNRAS, 498, 3503
Spruit H. C., 2002, A&A, 381, 923
Steiner A. W., Hempel M., Fischer T., 2013, ApJ, 774, 17
Summa A., Janka H.-T., Melson T., Marek A., 2018, ApJ, 852, 28
Takiwaki T., Kotake K., 2018, MNRAS, 475, L91
Takiwaki T., Kotake K., Foglizzo T., 2021, MNRAS, 508, 966
Tanabashi M. et al., 2018, Phys. Rev. D, 98, 030001
Tanaka M., Kato D., Gaigalas G., Kawaguchi K., 2020, MNRAS, 496, 1369
Timmes F. X., Swesty F. D., 2000, ApJS, 126, 501
Torres-Forné A., Cerdá-Durán P., Passamonti A., Obergaulinger M., Font J. A., 2019, MNRAS, 482, 3967
Tout C. A., Wickramasinghe D. T., Liebert J., Ferrario L., Pringle J. E., 2008, MNRAS, 387, 897
Usov V. V., 1992, Nature, 357, 472
Vartanyan D., Burrows A., 2020, ApJ, 901, 108
Vartanyan D., Burrows A., Radice D., Skinner M. A., Dolence J., 2019, MNRAS, 482, 351

Wanajo S., Sekiguchi Y., Nishimura N., Kiuchi K., Kyutoku K., Shibata M., 2014, ApJ, 789, L39
Watts A. L., Andersson N., Jones D. I., 2005, ApJ, 618, L37
Wickramasinghe D. T., Ferrario L., 2000, PASP, 112, 873
Woosley S. E., Baron E., 1992, ApJ, 391, 228
Yoon S.-C., Langer N., 2005, A&A, 435, 967
Yu Y.-W., Zhang B., Gao H., 2013, ApJ, 776, L40
Yu Y.-W., Li S.-Z., Dai Z.-G., 2015, ApJ, 806, L6
Yu Y.-W., Chen A., Wang B., 2019, ApJ, 870, L23
Yuan W., Zhang C., Chen Y., Ling Z., 2022, in Bambi C., Sangangelo A., eds, Handbook of X-ray and Gamma-ray Astrophysics. p. 86
Yuan W., et al., 2025, Sci. China Phys. Mech. Astron., 68, 239501
Zhu C., Pakmor R., van Kerkwijk M. H., Chang P., 2015, ApJ, 806, L1

This paper has been typeset from a TEX/LATEX file prepared by the author.